Ultramicroscopy 288 (2027) 114466

Contents lists available at ScienceDirect

Ultramicroscopy

journal homepage: www.elsevier.com/locate/ultramic

Thickness determination from EDXS maps acquired in a transmission electron microscope and its application for shape reconstruction of nanoparticles

Radian Popescu [a,*], Dagmar Gerthsen [a], Simon Hettler [a], Martin Peterlechner [a], Erich Müller [a], Damien Hudry [b], Yolita Maria Eggeler [a]

[a] Laboratory for Electron Microscopy (LEM), Karlsruhe Institute of Technology (KIT), Engesserstr. 7, 76131 Karlsruhe, Germany
[b] Institute of Microstructure Technology (IMT), Karlsruhe Institute of Technology (KIT), Hermann-von-Helmholtz-Platz 1, 76344 Karlsruhe Germany

ARTICLE INFO

Keywords:
3-dimensional shape reconstruction
energy dispersive X-ray spectroscopy
Thickness maps
Elemental mapping
Quantification
Cliff-Lorimer factors
Core-shell nanoparticles

ABSTRACT

This paper describes a method that can be applied for the three-dimensional (3D) reconstruction of nanoparticles (NPs) with convex shapes performed using a single 2D energy dispersive X-ray spectroscopy (EDXS) map recorded without any tilt in a transmission electron microscope. Data analysis is based on measured characteristic X-ray intensities of chemical elements chosen for the reconstruction that are transformed in their corresponding path lengths by using dedicated calibration factors. The method requires at least one measured calibration factor from which theoretical calibration factors can be calculated. By applying theoretical calibration factors, the method bears the potential to be a viable alternative to classical electron tomography. As advantages, this method can describe the shape of particles and their constituents located within agglomerates, when the substrate contaminates and when particle components contain elements with close atomic numbers. Moreover, it is not affected by missing wedge artifacts and does not require a tomography sample holder and dedicated software. Within this method, the 3D shape is symmetrically reconstructed along the electron-beam direction z from the NP center, which seems to restrict its applicability. However, many NPs synthesized under equilibrium conditions have convex, z-symmetrical shapes that can be reliably deduced from their 2D-projected shape on scanning TEM images. Even without assuming z-symmetrical shapes, the thickness in z-direction can always be evaluated. The method was applied to determine the 3D shape of a prismatic CeO_2-CaF_2 core-shell NP and an ellipsoidal $Au_{35}Co_{65}$ core-shell NP demonstrating its capability to deal with NPs having different morphologies and chemical compositions.

1. Introduction

Materials with dimensions between a few 10^{-9} and 10^{-7} m are usually denoted as nanoparticles (NPs) [1]. The last decade has opened the way to use NPs in many application fields, including nanocatalysis [2], medical imaging and drug delivery [3], fuel cells [4], solar cells [5], and memory storage devices [6]. All these application fields became possible after the development of NPs with optimized size and compositions. On the one hand, unlike bulk materials, the special physical and chemical properties of NPs remain strongly related to their small size, surface structure, and special shape [7]. On the other hand, recent investigations demonstrated that combining many chemical elements within a single structure yields an increase of its functionality, not only as a result of the combination of individual properties, but especially due to their close interaction within this single entity. Among all synthesized multicomponent NPs, particular attention was paid to two topologically different classes: core-shell (CS) [2] and asymmetric NPs, like Janus NPs, showing two different surface-segregated domains [8]. However, the increase of NP complexity has challenged their characterization to find the relationship between their special physical and chemical properties and the application performance.

Transmission electron microscopy (TEM) is one of the most important experimental tools for the investigation of the physical and chemical properties of nano-scaled materials. TEM yields 2-dimensional (2D) images with high resolution representing the projection of NPs on the image plane, which allows to determine their size, shape, size

* Corresponding author.
E-mail address: radian.popescu@kit.edu (R. Popescu).

https://doi.org/10.1016/j.ultramic.2026.114466
Received 24 February 2026; Received in revised form 27 October 2026; Accepted 29 October 2026
Available online 30 October 2026
0304-3991/© 2026 The Authors. Published by Elsevier B.V. This is an open access article under the CC BY license (http://creativecommons.org/licenses/by/4.0/).
Open access funding enabled and organized by Projekt DEAL.

distribution, and crystal structure. High-angle annular dark-field scanning TEM (HAADF-STEM) combined with energy-dispersive X-ray spectroscopy (EDXS) and/or electron energy-loss spectroscopy (EELS) yields the chemical composition and elemental distribution within heterostructures.

During the last decade, conventional electron tomography (ET) based on the HAADF-STEM imaging [9,10] has become the most advanced tool that can be applied to obtain a complete 3D characterization of the structure and chemical composition of nanomaterials, including core-shell, Janus-head, alloyed nanoparticles, etc. [11]. Possible mistakes by the interpretation of a single 2D image recorded from NPs are overcome by using HAADF-STEM ET, based on the acquisition of a series of 2D images of the same NP every few degrees (typically 1–3°) over a typical tilt range of −80° to +80°. The 2D images are aligned using cross-correlation procedures based on different approaches, and the shape is reconstructed using dedicated algorithms [12–16]. Classical ET requires the purchase of a tomography specimen holder and the installation and use of dedicated software, which are expensive. Moreover, despite its unique capabilities, the use of conventional ET is limited by the time required for the acquisition of a full tilt series of images taking about 15–60 min and, by that, cannot be used to study beam-sensitive NPs that do not withstand the long beam exposures. Another significant restriction in ET is given by the so-called "missing wedge", which results from the limited space in the TEM above and below the sample and the sample-holder geometry that restricts rotation and does not allow to record projection images within the ideal angular range of ± 90°. The missing wedge artifacts result in blurring, stretching, and distortions within the reconstructed image at those regions where 2D projections could not be acquired. Another limitation of the classical ET is related to the 3D characterization of particles within agglomerates, where, due to the small distances between particles, the tilt range of a given particle is drastically reduced due to overlap with its neighboring ones.

To get more insight into the properties of multi-component NPs with well-defined size, morphology, composition, and elemental distribution, multimodal tomography (MMT) was proposed as an alternative to the classical ET. Multimodal tomography implies the use of at least two different TEM techniques or "modes" to obtain 2D projections of a NP, which can then be reconstructed to obtain its 3D tomogram [11]. One notable example is the use of HAADF-STEM and EDXS modes (bimodal), where the 3D tomogram combines information obtained from 2D HAADF-STEM projected images, which are sensitive to both projection thickness and atomic number, with that from EDXS elemental maps showing the distribution of each chemical element within the particle [11,17]. We note that, similar to the classical HAADF-STEM tomography, to obtain the 3D EDXS elemental map of a NP, the acquisition of a tilt series of 2D maps is necessary, followed by their accurate alignment. However, the main drawback of HAADF-STEM/EDXS tomography is that, compared to HAADF-STEM imaging, EDXS mapping is hindered by a poor signal-to-noise ratio (SNR), which requires longer acquisition time and high electron doses, which can be critical for beam-sensitive particles. Even with the development of modern integrated EDXS detectors, such as Super-X, Dual-X, or Ultra-X detectors [18], which significantly reduce the acquisition time of 2D EDXS maps, shadowing remains a critical problem when aiming at the quantitative 3D EDXS reconstruction from tilt series.

This paper describes, for the first time to our knowledge, a method for the thickness determination and 3D-shape reconstruction of NPs with different chemical compositions and convex shapes by using a single 2D-EDXS elemental map recorded without any tilting, as a viable alternative to the classical ET and MMT, especially useful when the last two methods cannot be applied. The data analysis is based on the measured characteristic X-ray intensities of chemical elements that are chosen for the reconstruction, which are processed and transformed into corresponding path lengths through the particle along the electron-beam direction. The transformation is based on calibration factors from which the 3D reconstruction of the NP shape can be accomplished. These factors depend not only on the chemical composition and structure of the material under investigation, but also on the TEM used to perform the experiment, i.e., the electron beam (electron energy, beam current, probe size) and the EDXS detector characteristics. This requires as the first step, the determination of an experimental calibration factor of a given chemical element as a reference for the used TEM. Based on that, theoretical calibration factors of all other chemical elements can be calculated making the proposed technique an attractive alternative to the conventional ET or MMT. The method was applied to reconstruct the 3D shape of a prismatic beam-sensitive CeO_2-CaF_2 CS NP and an ellipsoidal $Au_{35}Co_{65}$ CS NP from their single 2D EDXS maps. Moreover, in the supporting information, further examples are presented, such as the thickness and the 3D-shape reconstruction of an amorphous SiO_2 particle, as well as the thickness map of an alloyed $Pt_{61}Pd_{39}$ NP with irregular shape. The particle selection was performed to demonstrate the capability of the 3D-shape reconstruction to deal with different structures, morphologies, and chemical compositions, as well as to emphasize some advantages compared with classical ET. One of the most important advantages we note is that, despite a moderately high electron dose of 68 pA/Å^2 used to record the EDXS map, the method remains well-suited for the 3D-shape reconstruction of beam-sensitive NPs within agglomerates that can be hardly investigated by classical ET. Another advantage is the lack of artifacts related to the missing-wedge or shadowing effects, like classical ET, being based on a single EDXS elemental map recorded without any tilting. This allows to reconstruct the 3D shape of NPs located within agglomerates, when their location is very close, but not overlapped with other NPs with the same chemical composition, which cannot be properly reconstructed by ET due to the small available angular range for the acquisition of the tilt series. The versatility and low cost of running this method are also mentioned, where the EDXS map acquisition is carried out using a standard single/double-tilt sample holder, and the data analysis is performed on a computer without special requirements regarding software and performance. Finally, it is mentioned that the method can be applied to reconstruct the 3D shape of NPs, when ET fails due to: 1) the substrate contamination yielding to a contrast increase of HAADF-STEM images during the acquisition of the tilt series, which is not related to the NP characteristics and 2) NPs with morphological constituents (core and shell) containing atoms with very close atomic numbers Z, which have about the same contrast on the HAADF-STEM images of the ET tilt series. However, the main limitation of our method is that the 3D NP shape is symmetrically reconstructed along the electron-beam direction z (symmetrical up-down reconstruction of the particle shape), which restricts its applicability to NPs with convex, z-symmetrical shapes. Although this restriction seems to limit its practical application, we note that NPs synthesized under equilibrium conditions in many systems are typically characterized by symmetrical convex polyhedral/ellipsoidal shapes [19–21]. NPs with concave regions are obtained either in the early stages of a fast anisotropic growth process or by coarsening of NPs with initial convex polyhedral shapes. However, a fast diffusion process of surface atoms toward regions with concave curvature, followed by atomic rearrangements in the NP volume, thermodynamically driven to assure the minimization of their surface free energy, takes place in such NPs [22,23]. They result, shortly after preparation and even after deposition on substrates, in NPs with convex polyhedral/ellipsoidal shapes [22,23]. For NPs grown under equilibrium conditions, the 2D shape of their x-y (in-plane) projection in HAADF-STEM images facilitates a reliable assessment of their real out-of-plane z-symmetry. This allows the use of the calculated thickness maps (x-y projection of NP thickness) for the 3D reconstruction of entire NP shapes by using a single EDXS map recorded without any tilt. However, for the 3D-shape reconstruction of NP constituents (i.e. the core and the shell of CS NPs), additional information about the shape of the core (convex, z-symmetric) and the core location within the NP is needed. As shown in the following, this can be obtained by using a single additional HAADF-STEM image of the NP recorded at a given tilt angle.

2. Experimental section

2.1. TEM specimen preparation and TEM experiments

Two reference specimens were prepared by a focused ion beam (FIB) from Pt and Mo evaporation targets. A small piece of each material was mounted in a Helios G4FX (Thermo Fisher Scientific) dual-beam instrument, and wedge-shaped TEM specimens were prepared and mounted on a standard Cu lift-out grid. The lamellae were thinned in a wedge shape with defined angles between 6–12°.

TEM samples of NPs were prepared at room temperature in air by drop casting a diluted NP suspension onto an ultrathin amorphous carbon film (3 nm) on holey carbon support film mounted on 400 μm mesh Cu grids (Ted Pella Inc.). The TEM samples were investigated by using a Gatan double-tilt holder (Gatan-Ametek, USA).

HAADF-STEM combined with EDXS experiments are conducted with a FEI Tecnai Osiris microscope (FEI, USA) at 200 keV electron energy, equipped with a high brightness X-FEG gun and a Super-X EDXS system comprising four silicon drift detectors. The four detectors are arranged around the optical axis of the transmission electron microscope with an elevation angle (for the center of each detector) of 22° and azimuth angles of 45°,135°, 225°, and 315°. The signals of the 4 detectors are summed before amplification and cannot be separated through post-processing.

Concentration profiles of different chemical elements within an object are determined from EDX spectra recorded in steps along a line scan (EDXS line scans) that passes through it (for NPs through their center). EDXS line scans are recorded by applying a drift-correction routine, which yields a local precision better than 1 nm by using a probe diameter of 3.0 ± 0.6 Å and a distance of 1 nm between two successive measuring points. EDX spectra are quantified with the FEI software package "TEM imaging and analysis" (TIA) version 4.7 SP3. Using TIA, element concentrations are calculated on the basis of a refined Kramers' law model, which includes corrections for detector absorption and background subtraction. For this purpose, standardless quantification, i.e., by means of theoretical sensitivity factors, without thickness correction was applied.

The 3D reconstruction of NP shapes is performed using their 2D EDXS elemental maps, which are quantified by using the ESPRIT software (version 2.3) from Bruker. The quantification is performed after applying corrections for detector absorption and background subtraction by using theoretical Cliff-Lorimer factors [24,25] without thickness correction.

2.2. Theoretical background

Cliff and Lorimer [24] proposed a simple relationship between the weight fractions, c_A and c_B of two elements A and B, and their detected characteristic X-ray intensities, I_A and I_B. For the chemical element A (and analogous for B), the generated characteristic X-ray intensity I'_A is given by [26]:

$$I'_A = I_0 \cdot \frac{K_A \cdot c_A \cdot Q_A \cdot \omega_A \cdot h_A \cdot t}{M_A} \tag{1}$$

where, I_0 is the incident electron beam current, K_A (u/cm^3, u: atomic mass unit) is a material dependent constant, Q_A (cm^2/atom) is the ionization cross-section for the element A, ω_A (dimensionless) is the fluorescence yield, i.e. the ionization fraction resulting in the emission of characteristic X-rays, h_A (dimensionless) is the relative intensity factor, i.e. the fraction of the total measured line intensity of the element A, t (cm) is the thickness of the specimen and M_A (u/atom) is the atomic weight of the element A [27]. However, I'_A as given by Eq. (1) is seldom measured, due to losses by absorption in the detector window and/or within the X-ray detector. All losses within the detector are taken into account by:

$$I_A = I'_A \cdot \varepsilon_A \tag{2}$$

where I_A is the measured characteristic X-ray intensity and ε_A is the detector efficiency for the element A. Combining Eqs. (1) and (2) yields a relation between the weight fraction c_A and the measured characteristic X-ray intensity I_A:

$$c_A = \frac{1}{K_A \cdot \frac{Q_A \cdot \omega_A \cdot h_A \cdot \varepsilon_A}{M_A} \cdot I_0} \cdot \frac{I_A}{t} \tag{3}$$

An analogous equation can be derived for the chemical element B:

$$c_B = \frac{1}{K_B \cdot \frac{Q_B \cdot \omega_B \cdot h_B \cdot \varepsilon_B}{M_B} \cdot I_0} \cdot \frac{I_B}{t} \tag{4}$$

The ratio of Eqs. (3) and (4) yields the relation between the weight concentrations c_A and c_B:

$$\frac{c_A}{c_B} = k_{A/B} \cdot \frac{I_A}{I_B} \tag{5}$$

where $k_{A/B}$ is the Cliff-Lorimer factor

$$k_{A/B} = \frac{k_A}{k_B} = \frac{K_B \cdot \frac{Q_B \cdot \omega_B \cdot h_B \cdot \varepsilon_B}{M_B}}{K_A \cdot \frac{Q_A \cdot \omega_A \cdot h_A \cdot \varepsilon_A}{M_A}} \tag{6}$$

Calculations in the following are based on values of Cliff-Lorimer factors $k_{A/Si}$ obtained after normalization to the Si-K line in our case, which are given in a database that is specific for the used TEM/EDXS system [25]. These factors are determined within the remote standard method for standardless analysis by assuming well-known measurement conditions, such as the electron energy, the incidence angle, the incident electron current, the take-off angle, and the EDXS efficiency [25]. Cliff-Lorimer $k_{A/B}$-factors for different other pairs of elements can be calculated according to [28]:

$$k_{A/B} = \frac{k_{A/Si}}{k_{B/Si}} \tag{7}$$

While theoretical calculations of Cliff-Lorimer $k_{A/Si}$-factors were reported to be affected by large systematic errors of about ±10%, their experimental measurement is more precise, resulting in errors of ±1%, but it is quite elaborate [29]. However, new theoretically calculated k-factors are more accurate, resulting in errors of less than ± 3% [27].

There is no standard formula for the calculation of the signal-to-noise ratio (SNR) in EDXS, because there are different methods for defining the "signal" and the "noise". Defining the "signal" as the peak intensity I_{peak} minus the intensity of the background under the peak I_b and the "noise" as the standard deviation of the background signal, such as the square root of the background counts, the SNR can be calculated according to:

$$SNR = \frac{I_{peak} - I_b}{\sqrt{I_b}} \tag{8}$$

By using this definition, SNR values better than $SNR \geq 4-5$ (typical $SNR \approx 20$) are determined for the quantification of EDX spectra recorded from small areas A_{elem}, while the quantification of EDX spectra recorded from wedge samples is characterized by $SNR \geq 100$ and $SNR \geq 20$ for incident electron-beam settings called spot size 6 and spot size 9 (see in the following).

3. Experimental results and discussion

3.1. Determination of calibration factors for the 3D-shape reconstruction

When the convergent electron beam in HAADF-STEM/EDXS experiments passes through an object, the measured characteristic X-ray intensities of each chemical element at a given (x_i, y_i) in-plane position on

the EDXS map is proportional to its local weight fraction at that position, the electron dose in the incident beam, and in the absence of absorption, will linearly increase with increasing path length through this object. Accordingly, a 2D EDXS elemental map of a small NP can be transformed into a 3D image. This can be achieved by using constant factors, denoted as calibration factors in the following, which allow to transform the measured characteristic X-ray intensities $I_{i,j}$ of each chemical element at a given (x_i,y_j) location on the 2D EDXS map in a local thickness $z_{i,j}(nm)$ at that position.

In the following, a procedure is proposed to determine such calibration factors, based on the quantification of EDXS line scans measured from wedge samples consisting of pure metals, which are obtained by FIB preparation from bulk materials. The wedge angles were chosen to be small, here of 6°, 8° and 12°, to assure a smooth increase of the wedge thickness with increasing distance from the edge. This results in extended regions with a linear thickness increase and a maximal thickness less than the mean free path of electrons with a given energy in the corresponding material, where absorption and fluorescence can be

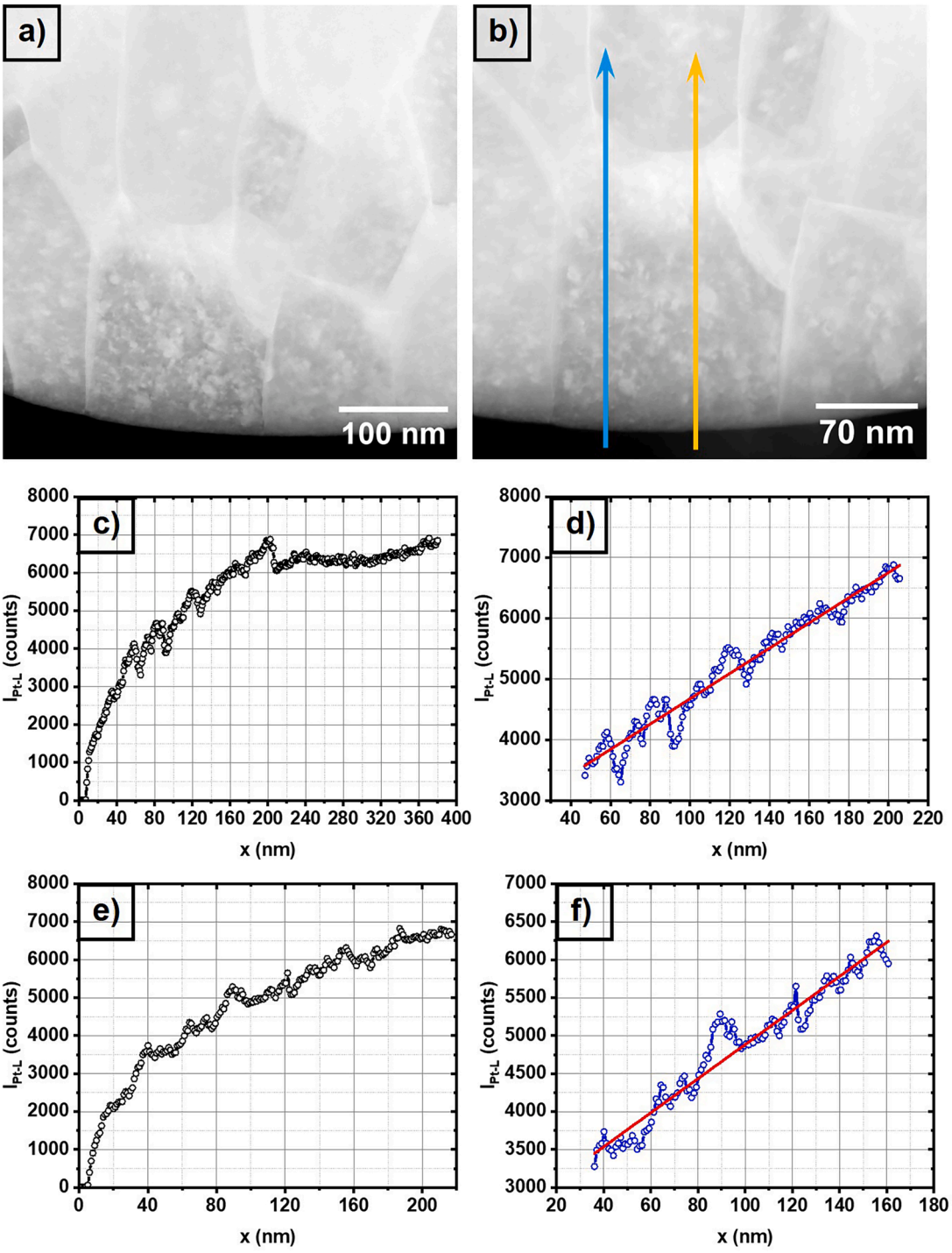


Fig. 1. a) HAADF-STEM image of the Pt wedge with a cutting angle of 6°; b) magnified region on the HAADF-STEM image in a) with orange and blue arrows showing the direction of EDXS line scans; c) and e) normalized experimental X-ray intensity of Pt-L series I_{Pt-L} as function of distance $x(nm)$ recorded along the orange (c) and blue (e) EDXS line scans; d) and f) selected regions with the linear increasing of $I_{Pt-L}(x)$ for the orange (d) and blue (f) EDXS line scans (blue symbols and lines) and their corresponding linear fits (red lines).

neglected. Wedges composed of pure Pt (face-centered-cubic (*fcc*) crystalline structure) and pure Mo (body-centered-cubic (*bcc*) structure) are considered for the determination of the structure dependency of the calibration factors. We note that these calibration factors will depend not only on the chemical composition and structure of the material under investigation, but also on the HAADF-STEM/EDXS system used to perform the experiment, i.e., the characteristics of the incident electron beam (probe size, electron energy, electron dose) and the EDXS detector (efficiency). Moreover, one can suppose that the calibration factor determination and the 3D-shape reconstruction could fail, when performed on oriented samples/NPs where channeling effects occur.

HAADF-STEM/EDXS experiments for determining the calibration factors and the acquisition of 2D EDXS maps were carried out using a well-defined incident electron beam (called spot size 6) characterized by an electron energy of 200 keV, a probe diameter of 3.0(±0.6) Å, and a beam current of 480(±12) pA. The effect of the change of the incident electron beam (on the same TEM) was investigated by determining calibration factors from HAADF-STEM/EDXS experiments performed on the same sample but using another incident electron beam (called spot size 9) characterized by a smaller probe size of 1.1(±0.2) Å and a smaller beam current of 64(±6) pA. In both experiments, the same C2 condenser aperture of 70 µm was used that allows the sample illumination by entire incident beam current.

The general application of the suggested 3D-reconstruction method first requires the determination of experimental calibration factors from wedge specimens with well-known thickness profile and chemical composition. Combining all the information obtained after the investigation of a limited number of wedge samples with well-known properties, the basis for the theoretical calculation of calibration factors for all other elements can be derived (cf. Sect. 3.1.3). Only by the use of such theoretical calibration factors, the widespread application of the suggested 3D-shape reconstruction method is enabled.

3.1.1. Experimental calibration factors for Pt and Mo

In the following, the determination of experimental calibration factors is described. It is based on the evaluation of the linearly increasing measured X-ray intensity of the Pt-L and Mo-L series, respectively, with increasing wedge thickness, as determined after the quantification of their EDXS line scans.

The HAADF-STEM image (Fig. 1a) shows a region on the Pt wedge with a cutting angle of 6°, from where two EDXS line scans were acquired to determine the Pt calibration factor (orange and blue arrows on Fig. 1b). EDXS line scans were recorded by using an electron beam with spot size 6 (probe diameter of 3.0 Å, incident beam current of 480 pA), a distance of 1 nm between two successive measuring points and 3 s acquisition time for each spectrum along the line scan. Each EDX spectrum was then normalized to correspond to 1 s acquisition time. The graph of the normalized measured X-ray intensity of the Pt-L series I_{Pt-L} determined after the quantification of the EDXS line scan (orange arrow on Fig. 1b), shows, just after the steep increase at the wedge edge as an artifact of the FIB cutting process, a region with a linearly increasing of I_{Pt-L} with increasing distance from the edge $x(nm)$, i.e., with the wedge thickness (Fig. 1c). The Pt calibration factor for the 3D reconstruction $q_{Pt-L}(counts/nm)$ is then evaluated from the slope m of the linear fit of measured intensities I_{Pt-L} as function of the distance $x(nm)$ within this linear region according to the following relation:

$$tan(6^{\circ}) = \frac{\Delta I_{Pt-L}/q_{Pt-L}}{\Delta x} = \frac{m}{q_{Pt-L}} \tag{9}$$

The linear region of $I_{Pt-L}(x)$ is selected according to two main criteria: 1) it starts after the end of the FIB-cutting artifact region at the wedge edge, assuring by that an as thin as possible thickness along the entire linear region; 2) it ends in the vicinity of the grain boundary, when the slope of the linear region of $I_{Pt-L}(x)$ changes due to density (structure)/composition (impurities) changes and further consideration of points along the EDXS scan yielding a worsening of the linear fit quality described by the R^2-value by ~5%.

The linear fit of the measured intensities I_{Pt-L} as function of the distance $x(nm)$ (Fig. 1d) ($R^2 = 0.957$) is described by:

$$I_{calc}(x) = 2596.9 + 20.8 \cdot x \tag{10}$$

and results in a slope $m = 20.8 \pm 0.4$ $(counts/nm)$ and a calibration factor of

$$q_{Pt-L} = \frac{20.8 \pm 0.4}{\tan(6^{\circ})} = 197.8 \pm 3.8 \ (counts/nm) \tag{11}$$

Oscillations of the measured I_{Pt-L} around the linear fitted values given by Eq. (9) by about 5–7% are related to the local thickness variations induced by the FIB cutting of the wedge, which yields a quite precise cutting angle of 6° over longer distances, but may show slightly varying values on a smaller scale.

The error of the factor q_{Pt-L} induced by the small imprecision in the wedge cutting angle was determined by calculating q_{Pt-L} using the linear region of I_{Pt-L} as function of distance $x(nm)$ (Fig. 1e) measured from another EDXS line scan recorded at a different position on the same wedge (blue arrow on Fig. 1b). The linear fit ($R^2 = 0.946$) (Fig. 1f) is described by the relation:

$$I_{calc}(x) = 2640.5 + 22.4 \cdot x \tag{12}$$

and results in a value of $q_{Pt-L} = 213.5 \pm 4.1$ $(counts/nm)$. In the following calculation, the average value $q_{Pt-L} = 205.7 \pm 10.1$ $(counts/nm)$ for the Pt calibration factor will be considered.

HAADF-STEM images in Fig. 2a and b show the magnified region of two Mo wedges with cutting angles of 8° and 12°, respectively, from where EDXS line scans were recorded (arrows in Fig. 2a, and b) to determine the Mo calibration factor $q_{Mo-L}(counts/nm)$. EDXS line scans were acquired with the same experimental conditions as for the Pt wedge. Graphs of the measured characteristic X-ray intensity of the Mo-L series I_{Mo-L} determined after the quantification of the EDXS line scans show, just after the steep increase at the wedge edge, a region with a linear increase of I_{Mo-L} with increasing distance from the wedge edge $x(nm)$, i.e., with the wedge thickness (Fig. 2c and d). The Mo calibration factor for the 3D reconstruction $q_{Mo}(counts/nm)$ is evaluated from the slope m of the linear fit of measured normalized intensities I_{Mo-L} as function of distance $x(nm)$ from the edge of each wedge (Fig. 2e, and f).

The evaluation of the linear region of the EDXS line scan recorded from the Mo wedge with 8° cutting angle results in the linear fit ($R^2 = 0.989$) (Fig. 2e):

$$I_{calc}(x) = 464.9 + (22.2 \pm 0.2) \cdot x \tag{13}$$

and a Mo calibration factor of

$$q_{Mo-L} = \frac{22.2 \pm 0.2}{\tan(8^{\circ})} = 157.8 \pm 1.4 \ (counts/nm) \tag{14}$$

while the evaluation of the linear region of the EDXS line scan recorded from the 12° wedge yields the linear fit ($R^2 = 0.997$) (Fig. 2f):

$$I_{calc}(x) = 284.6 + (34.6 \pm 0.2) \cdot x \tag{15}$$

and consequently, to a Mo calibration factor of

$$q_{Mo-L} = \frac{34.6 \pm 0.2}{\tan(12^{\circ})} = 162.6 \pm 0.9 \ (counts/nm) \tag{16}$$

Then, the average q_{Mo} calibration factor can be calculated as $q_{Mo-L} = 160.2 \pm 3.5$ $(counts/nm)$.

3.1.2. Calibration factor dependence on the incident electron beam

The effect of the incident electron beam on the calibration factors

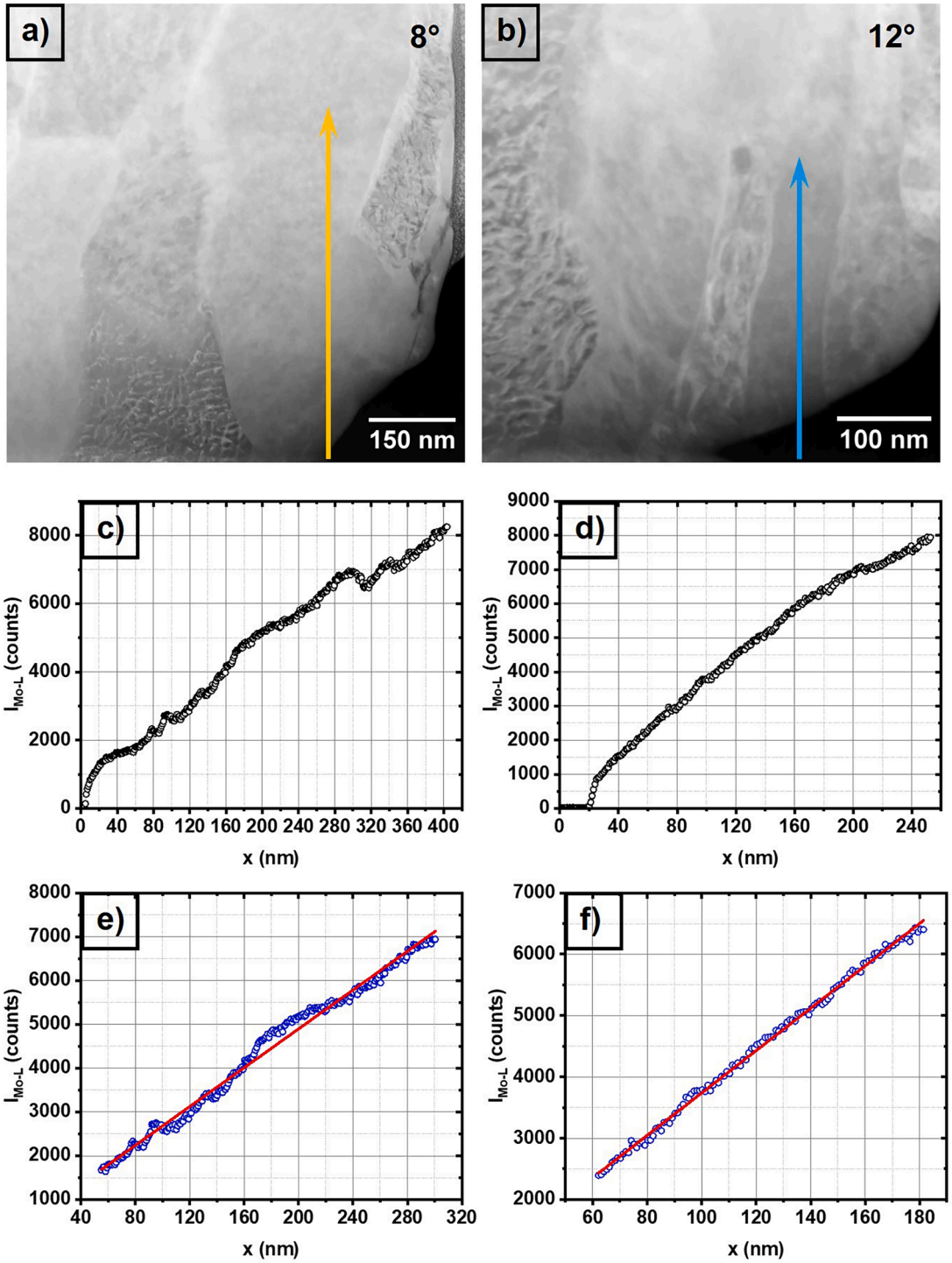


Fig. 2. a)-b) HAADF-STEM images of Mo wedges with cutting angles of (a) 8° and (b) 12° with orange and blue arrows showing the direction of EDXS line scans; c)-d) experimental normalized X-ray intensity of the Mo-L series I_{Mo-L} as function of distance $x(nm)$ recorded along the orange (c) and blue (d) EDXS line scans; e) - f) selected regions with the measured linear increasing of $I_{Pt-L}(x)$ for the orange (e) and blue (f) EDXS line scans (blue symbols and lines) and their corresponding linear fits (red lines).

was investigated by performing HAADF-STEM/EDXS experiments on the same TEM, but using an incident beam with modified characteristics. For that, EDXS line scans were recorded from the same region on the Pt wedge with the 6° cutting angle by using the spot size 9 (reduced diameter of 1.1(±0.2) Å and beam current of 64 pA), a distance of 1 nm between two measuring points, and 3 s acquisition time for each spectrum. Each EDX spectrum was then normalized to correspond to a 1 s acquisition time.

The graph of the measured characteristic X-ray intensity of the Pt-L series I_{Pt-L} after the quantification of the EDXS line scan recorded from the position marked by the orange arrow in Fig. 1b, shows a region with a linear increase of I_{Pt-L} with increasing distance from the wedge edge $x(nm)$ (Fig. 3a). The evaluation of the linear region of the EDXS line scan results in the linear fit ($R^2 = 0.954$) (Fig. 3c):

$$I_{calc}(x) = 228.34 + (2.52 \pm 0.07) \cdot x \quad (17)$$

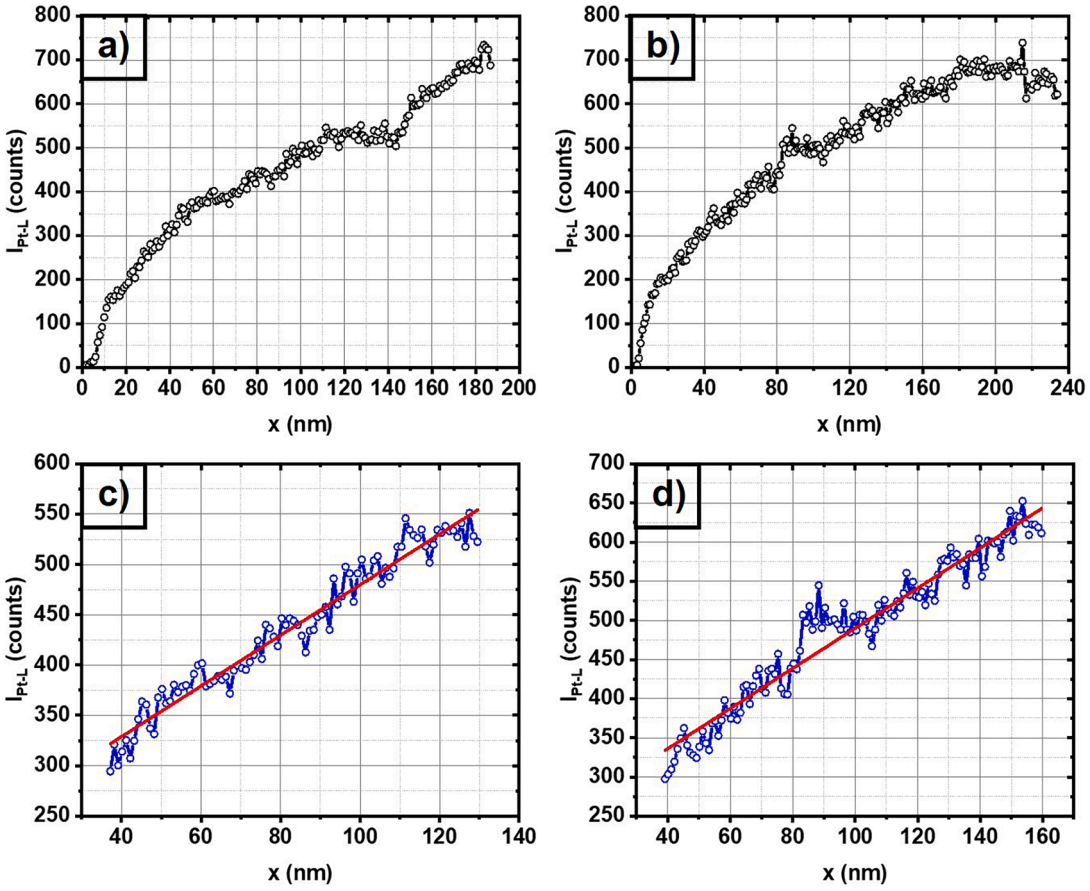


Fig. 3. a)-b) Experimental normalized characteristic X-ray intensity of the Pt-L series I_{Pt-L} as function of distance $x(nm)$ recorded along the orange (a) and blue (b) EDXS line scans in Fig. 1b by using an electron beam with a beam size of 1.1 Å; c)-d) selected regions with linear increasing $I_{Pt-L}(x)$ for the orange (c) and blue (d) EDXS line scans (blue symbols and lines) and their corresponding linear fits (red lines).

and a Pt calibration factor of

$$q^{*}_{Pt-L} = \frac{2.52 \pm 0.07}{\tan(6^{\circ})} = 23.9 \pm 0.7 \ (counts\,/\,nm) \tag{18}$$

Similarly, the evaluation of the linear region of the measured X-ray intensity of the Pt-L series I_{Pt-L} determined after the quantification of the EDXS line scan recorded from the position marked with the blue arrow in Fig. 1b (Fig. 3b), results in the linear fit ($R^2 = 0.940$) (Fig. 3d):

$$I_{calc}(x) = 233.64 + (2.56 \pm 0.06)\cdot x \tag{19}$$

and a calibration factor of Pt-L series of:

$$q^{*}_{Pt-L} = \frac{2.56 \pm 0.06}{\tan(6^{\circ})} = 24.4 \pm 0.6 \ (counts\,/\,nm) \tag{20}$$

This yields an average calibration factor for Pt-L of $q^{*}_{Pt-L} = 24.2 \pm 0.7 \ (counts\,/nm)$.

The experiment demonstrates that, as expected, the experimental calibration factors of Pt-L q^{*}_{Pt-L} and q_{Pt-L} are proportional to the incident beam current used in the corresponding HAADF-STEM/EDXS experiments.

3.1.3. Theoretical method to calculate the experimental calibration factors

The experimental determination of calibration factors for the 3D-shape reconstruction from 2D EDXS maps using wedge samples as described above, is tedious and in many cases not possible due to the difficulty to prepare wedges composed of pure elements. However, developing a theoretical method to calculate calibration factors for all chemical elements based on the precise measurement of a very few, or even of a single calibration factor may open the possibility of a widespread application of this method for the 3D-shape reconstruction of NPs and make it a viable addition to the classical ET and MMT.

A theoretical method, which calculates calibration factors from EDXS maps recorded with an incident electron beam having defined characteristics (beam size and current), is based on the fact that: 1) the measured characteristic X-ray intensity of an arbitrary chemical element at a given in-plane position (x_i,y_j) within an EDXS map is proportional to its local weight concentration $c_{wt}\left(x_i,y_j\right)$ (cf. Eqs. (3,4)) and 2) the EDXS quantification yields weight compositions, which are averaged along the electron-beam direction, i.e., the whole volume along the electron trajectory contributes to the detected X-ray signal. However, Eqs.(3,4) contain the properties $Q_{A,B}$, $\omega_{A,B}$ and $h_{A,B}$, which can be in general not accurately calculated. This means that the evaluation of thicknesses by comparison of measured with calculated X-ray intensities would be inaccurate. On the other hand, Cliff-Lorimer factors are provided in the database delivered with the EDXS system [25], which are routinely used to quantify EDX spectra with good accuracy. It is therefore desirable to make use of Cliff-Lorimer factors for thickness determinations. In the following, we will show how Cliff-Lorimer factors provided with the used EDXS system can be applied for the calculation of calibration factors and the evaluation of local thicknesses.

An incident electron beam with a beam diameter $b_{beam} = 3.0(\pm 0.6)$ Å and a beam current of $I_0 = 480\ pA$ (spot size 6) was used for the experimental determination of the calibration factors of Pt and Mo described in Sect. 3.1.1, which illuminates a surface with the area

$$S_{beam} = \pi\cdot\left(\frac{b_{beam}}{2}\right)^2 = 7.069\ \text{Å}^2 \tag{21}$$

This results in a beam current density j_0 of

$$j_0 = \frac{I_0}{S_{beam}} = 67.902\ \frac{pA}{\mathring{A}^2} \tag{22}$$

The weight concentration of crystalline Pt with a *fcc* structure and the unit cell with a volume V_{uc}^{Pt} can be calculated taking into account that the unit cell contains $n_{Pt} = 4$ Pt atoms, its lattice parameter is $a_{Pt} = 3.923$ Å and Pt atoms have an atomic weight of $M_{Pt} = 195.078\ u$:

$$c_{Pt}^{wt} = \frac{n_{Pt}\cdot M_{Pt}}{V_{uc}^{Pt}} = \frac{4\cdot 195.078}{3.923^3} = 12.924\ u \Big/ \mathring{A}^3 \tag{23}$$

The theoretical calculation of calibration factors for the 3D-shape reconstruction is based on the relationship between the weight fraction c_{Pt}^{wt} of the Pt illuminated by the electron beam propagating along a_{Pt} through the wedge and the measured characteristic X-ray intensity of the Pt-L series I_{Pt-L}. To find this relation, the experimental calibration factor for the 3D reconstruction of Pt-L series q_{Pt-L} $(counts/nm)$ using a 3 Å beam diameter (spot size 6) recalculated for a path with the $a_{Pt}(nm)$ length

$$q'_{Pt-L} = q_{Pt-L}\cdot a_{Pt} = 80.696\ counts\ for\ the\ path\ length\ a_{Pt} \tag{24}$$

is used. Expressing Eq. (3) for Pt and the path length a_{Pt} yields

$$c_{Pt}^{wt}\cdot a_{Pt} = \frac{1}{K_{Pt}\cdot\frac{Q_{Pt}\cdot\omega_{Pt}\cdot h_{Pt}\cdot\varepsilon_{Pt}}{M_{Pt}}\cdot I_0}\cdot\left(\frac{I_{Pt-L}}{t}\right)\cdot a_{Pt} \tag{25}$$

or, rewritten for the beam current density j_0 to

$$c_{Pt}^{wt}\cdot a_{Pt}\cdot S_{beam} = \frac{1}{K_{Pt}\cdot\frac{Q_{Pt}\cdot\omega_{Pt}\cdot h_{Pt}\cdot\varepsilon_{Pt}}{M_{Pt}}\cdot j_0}\cdot\left(\frac{I_{Pt-L}}{t}\right)\cdot a_{Pt} \tag{26}$$

Taking into account that a volume of

$$V_{beam}^{Pt} = S_{beam}\cdot a_{Pt} = 27.732\ \mathring{A}^3 \tag{27}$$

will be irradiated by the electron beam, which propagates a distance corresponding to the Pt-lattice parameter $a_{Pt} = 3.923$ Å, the weight fraction illuminated by the electron beam along the distance a_{Pt} can be expressed by:

$$c_{Pt}^{wt}\cdot V_{beam}^{Pt} = f_{Pt}\cdot n_{Pt}\cdot M_{Pt} = 358.358\ u\ for\ the\ path\ length\ a_{Pt} \tag{28}$$

where

$$f_{Pt} = \frac{V_{beam}^{Pt}}{V_{uc}^{Pt}} = \frac{27.732}{3.923^3} = 0.4593 \tag{29}$$

is the fraction of the unit cell volume illuminated by the incident electron beam. Then, Eq. (26) can be written as

$$c_{Pt}^{wt}\cdot V_{beam}^{Pt} = \frac{1}{K_{Pt}\cdot\frac{Q_{Pt}\cdot\omega_{Pt}\cdot h_{Pt}\cdot\varepsilon_{Pt}}{M_{Pt}}\cdot j_0}\cdot\left(\frac{I_{Pt-L}}{t}\right)\cdot a_{Pt} = w_{Pt-L}^{exp}\cdot q_{Pt-L}\cdot a_{Pt} \tag{30}$$

for the path length $a_{Pt}(nm)$, where an experimental factor of Pt-L series w_{Pt-L}^{exp} is defined according to:

$$w_{Pt-L}^{exp} = \frac{1}{K_{Pt}\cdot\frac{Q_{Pt}\cdot\omega_{Pt}\cdot h_{Pt}\cdot\varepsilon_{Pt}}{M_{Pt}}\cdot j_0} = \frac{k_{Pt-L}}{j_o} \tag{31}$$

with $k_{Pt-L} = \frac{M_{Pt}}{K_{Pt}\cdot Q_{Pt}\cdot\omega_{Pt}\cdot h_{Pt}\cdot\varepsilon_{Pt}}$. From Eq. (30), w_{Pt-L}^{exp} can be explicitly calculated:

$$w_{Pt-L}^{exp} = \frac{c_{Pt}^{wt}\cdot V_{beam}^{Pt}}{q'_{Pt-L}} = 4.441\ (u/counts) \tag{32}$$

Using the factor w_{Pt-L}^{exp}, the calibration factor of Pt-L series q'_{Pt-L} is expressed by:

$$q'_{Pt-L} = \frac{c_{Pt}^{wt}\cdot V_{beam}^{Pt}}{w_{Pt-L}^{exp}} = \frac{V_{beam}^{Pt}}{V_{uc}^{Pt}}\cdot\frac{n_{Pt}\cdot M_{Pt}}{w_{Pt-L}^{exp}} (= 80.696)\ counts\ for\ the\ path\ length\ a_{Pt} \tag{33}$$

In the following, the factor w_{Mo-L}^{exp} of the Mo-L series will be calculated by using the experimental calibration factor of Mo-L series q'_{Mo-L}. For the Mo wedge an illuminated volume of

$$V_{beam}^{Mo} = S_{beam}\cdot a_{Mo} = 22.233\ \mathring{A}^3 \tag{34}$$

is calculated for crystalline *bcc* Mo with $a_{Mo} = 3.1451$ Å. For the unit cell of Mo with a volume of V_{uc}^{Mo}, the fraction of the unit cell illuminated by the electron beam f_{Mo} is

$$f_{Mo} = \frac{V_{beam}^{Mo}}{V_{uc}^{Mo}} = 0.7147 \tag{35}$$

Taking into account that each unit cell of crystalline *bcc* Mo contains $n_{Mo} = 2$ Mo atoms, a corresponding weight fraction of Mo atoms illuminated by the electron beam

$$c_{Mo}^{wt}\cdot V_{beam}^{Mo} = f_{Mo}\cdot n_{Mo}\cdot M_{Mo} = 137.098\ u\ for\ the\ path\ length\ a_{Mo} \tag{36}$$

can be calculated for Mo atoms with an atomic mass of $M_{Mo} = 95.94\ u$. Then, the experimental calibration factor for the 3D reconstruction of Mo-L series q_{Mo-L} $(counts/nm)$ recalculated for a path with the $a_{Mo}(nm)$ length is

$$q'_{Mo-L} = q_{Mo-L}\cdot a_{Mo} = 50.385\ counts\ for\ the\ path\ length\ a_{Mo} \tag{37}$$

An experimental factor for Mo-L series w_{Mo-L}^{exp} can be calculated according to Eq. (30):

$$w_{Mo-L}^{exp} = \frac{c_{Mo}^{wt}\cdot V_{beam}^{Mo}}{q'_{Mo-L}} = 2.721\ (u/counts) \tag{38}$$

Alternatively, a calculated factor w_{Mo-L}^{calc} can be determined by using the experimental value of w_{Pt-L}^{exp} (Eq. (32)), Eq (7), and the Cliff-Lorimer factors $k_{Pt-L/Si} = 4.446$ and $k_{Mo-L/Si} = 2.588$ from the database in Ref. [25], which contains the Cliff-Lorimer factors with reference to silicon.

$$\frac{w_{Mo-L}^{calc}}{w_{Pt-L}^{exp}} = \frac{k_{Mo-L}/j_0}{k_{Pt-L}/j_0} = \frac{k_{Mo-L/Si}}{k_{Pt-L/Si}} \xrightarrow{yields} w_{Mo-L}^{calc} = w_{Pt-L}^{exp}\cdot\frac{k_{Mo-L/Si}}{k_{Pt-L/Si}} = 2.586 \tag{39}$$

with $k_{Mo-L} = \frac{M_{Mo}}{K_{Mo}\cdot Q_{Mo}\cdot\omega_{Mo}\cdot h_{Mo}\cdot\varepsilon_{Mo}}$. The calculated w_{Mo-L}^{calc} is in good agreement with the experimental value of w_{Mo-L}^{exp} in Eq. (38) (i.e. 5% smaller) and will be used to determine a theoretical calibration factor for the Mo-L series q_{Mo-L}^{calc}

$$q_{Mo-L}^{calc} = \frac{V_{beam}^{Mo}}{V_{uc}^{Mo}}\cdot\frac{n_{Mo}\cdot M_{Mo}}{w_{Mo-L}^{calc}} = 53.015\ counts\ for\ the\ path\ length\ a_{Mo} \tag{40}$$

which agrees within 5% with the experimental value q'_{Mo-L}.

In Sect. 3.1.2, a convergent electron beam with a reduced beam size of $1.1(\pm 0.2)$ Å and electron current of $I_o^* = 64\ pA$ (spot size 9), was used for the experimental determination of the calibration factor q_{Pt-L}^* of the Pt-L series. Also in this case, a comparison between the experimental and calculated calibration factors of the Pt-L series will be performed to support the use of theoretical q^{calc} factors for the 3D-shape reconstruction.

The electron beam with 1.1 Å diameter is characterized by the corresponding illuminated surface is of $S_{beam}^* = 0.9503\ \mathring{A}^2$ and a beam current density of $j_0^* = 67.37\ pA/\mathring{A}^2$. A volume of

$$V_{beam}^{Pt*} = S_{beam}^*\cdot a_{Pt} = 3.728\ \mathring{A}^3 \tag{41}$$

will be irradiated by the electron beam by propagating a distance a_{Pt}

through the Pt wedge. The fraction of the Pt unit cell illuminated by the electron beam of $f^*_{Pt} = \frac{V^{Pt*}_{beam}}{V^{Pt}_{uc}} = 0.06175$ yields a weight fraction of illuminated Pt atoms of

$$c^{wt*}_{Pt} \cdot V^{Pt*}_{beam} = f^*_{Pt} \cdot n_{Pt} \cdot M_{Pt} = 48.184\ u \text{ for the path length } a_{Pt} \quad (42)$$

A calculated w^{calc*}_{Pt-L} factor can be determined accordingly to

$$\frac{w^{calc*}_{Pt-L}}{w^{exp}_{Pt-L}} = \frac{k_{Pt-L}/j^*_0}{k_{Pt-L}/j_0} = \frac{j_0}{j^*_0} \xrightarrow{yields} w^{calc*}_{Pt-L} = w^{exp}_{Pt-L} \frac{j_0}{j^*_0} = 4.476\ u \Big/ counts \quad (43)$$

which is in fair agreement with the experimental value of $w^{exp}_{Pt-L} = 4.441\ (u/counts)$ given in Eq. (32), due to similar beam current densities of spot size 6 and 9. The characteristic X-ray intensity of the Pt-L series expected to be measured from the weight fraction c^{wt*}_{Pt} along the path length a_{Pt} through the Pt wedge is

$$q^{calc*}_{Pt-L} = \frac{c^{wt*}_{Pt} \cdot V^{Pt*}_{beam}}{w^{calc*}_{Pt-L}} = 10.765\ counts \text{ for the path length } a_{Pt} \quad (44)$$

which is in fair agreement with the experimental calibration factor of Pt-L series $q^{'*}_{Pt-L} = 9.5\ counts$ obtained for a propagation distance $a_{Pt}(nm)$ through the wedge.

Summarizing all, the theoretical calibration factor for the 3D-shape reconstruction of a given chemical element A by using its characteristic X-ray series R can be calculated using Eqs. (39) und (43) as:

$$q^{calc}_{A-R} = \frac{V^A_{beam}}{V^A_{uc}} \cdot \frac{n_A \cdot M_A}{\left(w^{exp}_{B-T} \cdot \frac{k_{A-R/St}}{k_{B-T/St}} \frac{j^B_0}{j^A_0} \right)}\ counts \text{ for the path length } a_A(nm) \quad (45)$$

where $V^A_{beam} = S_{beam} \cdot a_A$ is the volume irradiated by the electron beam that propagates along a distance $a_A(nm)$, where a_A is the lattice parameter along the z-direction (the electron-beam direction). V^A_{uc} is the volume of the A unit cell, n_A is the number of A atoms within the unit cell, M_A is the atomic mass of A in u. $k_{A-R/St}$ and $k_{B-T/St}$ are Cliff-Lorimer factors (normalized to the standard chemical element "*St*") of the characteristic X-ray series/lines R/T of the element A/B from the database specific for the TEM-EDXS system experimentally used, w^{exp}_{B-T} is the measured factor of the B-T series/line, which has to be previously determined from a wedge sample and j^A_0 and j^B_0 are incident beam current densities used for recording the EDXS map of the element A and for recording the EDXS line scan of the wedge sample composed of the element B, respectively. We note that the use of the same TEM-EDXS system with the same incident beam characteristics, i.e. spot size 6, for recording both, the EDXS line scan of the wedge sample and the EDXS map for the 3D reconstruction, yields the same incident beam current densities j^A_0 and j^B_0 in Eq. (45). The case of a non-cubic unit cell is detailed in Sect. 3.3.

The method described here can be generalized to calculate theoretical calibration factors of amorphous materials for their 3D-shape reconstruction. The extended formalism and its application to visualize the shape of an amorphous SiO_2 NP are presented in the supporting information.

In summary, the good agreement of the measured and theoretically calculated calibration factors facilitates their use for the thickness determination of objects with crystalline/amorphous structure containing arbitrary chemical elements. We note the increase of the discrepancy between the experimental and the calculated calibration factorswhen decreasing the electron beam diameter, from 5% for a beam diameter of 3.0 Å up to about 10% for a small beam with a diameter of about 1.1 Å.

This is mainly related to an increasing relative error $\varepsilon(\%)$ of the experimental calibration factor due to lower counting statistics, when incident electron beams with decreasing currents I (beam diameters) are used. The effect can be quantified by calculating the relative error $\varepsilon(\%)$ made by the integration of the characteristic X-ray intensity of the Pt-L series I_{Pt-L} after background subtraction, which is given by $\varepsilon = 3/\sqrt{I_{Pt-L}}$. The I_{Pt-L} intensity chosen for the evaluation was measured at the beginning of the linear increasing region of the EDXS line scans recorded on the Pt wedge sample with a cutting angle of 6° (Fig. 1b) by using the two incident electron beams with diameters 3.0 ± 0.6 Å and 1.1 ± 0.2 Å (called spot size 6 and 9).

Accordingly, the quantification of the EDX spectrum acquired with spot size 6 at $x = 47\ nm$, which is the starting point of the linear increasing region (Fig. 1d) of the EDXS line scan in Fig. 1b (orange arrow), yields, after background subtraction, an integrated intensity of the Pt-L series of $I_{Pt-L}(x = 47\ nm) = 9289\ counts\ in\ 3\ s$ (each EDX spectrum was acquired for 3 s), which corresponds to an error of $\varepsilon = 3.11$ %. A similar error $\varepsilon = 3.05$ % is obtained for the evaluation of the EDX spectrum at $x = 37\ nm$ (integrated intensity of $I_{Pt-L}(x = 37\ nm) = 9649\ counts\ in\ 3\ s$), which is the starting point of the linear increasing region (Fig. 1f) on the second EDXS line scan recorded with spot size 6 (blue arrow in Fig. 1b). By using the incident electron beam called spot size 9, the quantification of the EDX spectrum at $x = 38\ nm$, the beginning of the linear increasing region of the EDXS line scan (Fig. 3c) recorded from the Pt wedge sample (orange arrow in Fig. 1b), results, after background subtraction, in an integrated I_{Pt-L} value of $I_{Pt-L}(x = 38\ nm) = 782\ counts\ in\ 3\ s$ corresponding to $\varepsilon = 10.73$ %. A similar value $\varepsilon = 10.67$ % is obtained for the evaluation of the EDX spectrum at $x = 44\ nm$ (integrated intensity of $I_{Pt-L}(x = 44\ nm) = 791\ counts\ in\ 3\ s$), which is the starting point of the linear increasing region (Fig. 3d) on the EDX spectrum recorded along the second EDXS line scan (blue arrow in Fig. 1b).

Although $SNR > 20$ describe well-defined peaks in the EDX spectra, the integrated I_{Pt-L} after background subtraction used to calculate the experimental calibration factors of Pt, is affected by a large error of $\varepsilon \approx 10$ % due to low counting statistics for an incident electron beam with a small beam current and a small beam diameter of 1.1(±0.2) Å. Moreover, we note that the maximal errors of about $\varepsilon = 3$ % and $\varepsilon = 10$ % for the experimental I_{Pt-L} by using electron beams with a large and small diameter correspond to the discrepancy between the experimental and theoretically calculated calibration factors of 5% and 10%. This supports the important role of the counting statistics on the precision of the experimentally determined calibration factors of Pt and largely explains their discrepancies with the calculated values.

The decreasing error of the 3D-shape reconstruction with increasing counting statistics (incident beam diameter) suggests that reliable thickness calculation and shape reconstructions can be obtained using electron beam diameters of $b_{beam} \geq 1$ Å, which assure a good counting statistic. The dependency of theoretical calibration factors on the corresponding Cliff-Lorimer factors, which are characteristic for the particular used TEM-EDXS system, together with information about the chemical composition of the investigated material and the electron beam characteristics (diameter and current), allow to extend the applicability of this method to the thickness determination of objects based on their 2D EDXS maps recorded on arbitrary TEMs equipped with a suitable EDXS system. However, before applying the method on a new microscope, at least one experimental calibration factor must be determined by using a wedge sample.

3.2. Thickness and 3D-shape reconstruction of a CeO_2-CaF_2 core-shell nanoparticle

In the following, the thickness and the 3D-shape reconstruction of prismatic CeO_2-CaF_2 CS NPs will be demonstrated. The HAADF-STEM image and the corresponding EDXS elemental maps of Ca (Ca-K series), Ce (Ce-L series), and the superposition of the Ca and Ce maps for several CeO_2-CaF_2 CS NPs show the CS morphology of these NPs with rectangular 2D projections (Fig. 4). The rectangular orange frame in Fig. 4a marks the single CeO_2-CaF_2 CS NP selected for the thickness/3D-

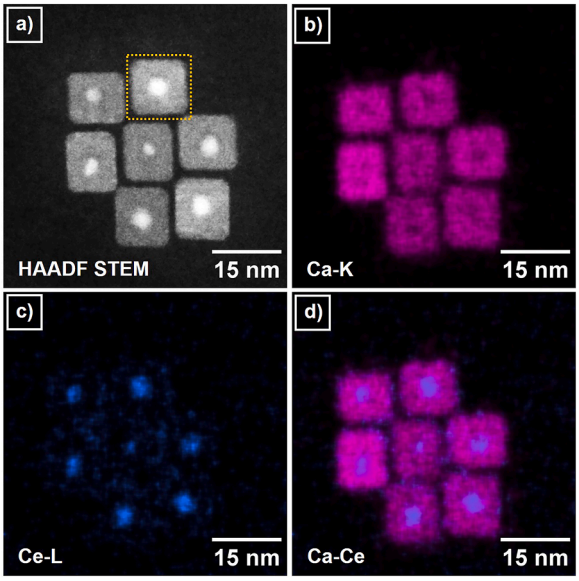


Fig. 4. CeO_2-CaF_2 CS NPs: a) HAADF-STEM image with yellow dashed frame marking the NP selected for the 3D shape reconstruction; (b)-(d) corresponding EDXS elemental maps of (b) Ca (Ca-K series pink), (c) Ce (Ce-L series blue), and (d) superposition of the Ca and Ce maps.

shape reconstruction, which have a chemical composition of $Ca_{26\pm1}F_{51\pm1}Ce_{7\pm1}O_{16\pm1}$ (in a good approximation CeO_2-CaF_2) obtained by the quantification of its EDXS map. The EDXS map was recorded during an illumination of about 40 s with the electron beam characterized by a moderate electron dose of ≈68 pA/Å^2 (spot size 6), showing that our approach is suitable to obtain thickness maps of agglomerated, beam-sensitive NPs.

3.2.1. *Experimental set-up for the acquisition of 2D EDXS elemental maps*

The experimental parameters used to record the 2D EDXS elemental map can be found in the general information about the map acquisition and are delivered by the ESPRIT software. Important for the thickness determination of the NP are:

- Pixel size: $a_p = 0.76$ Å
- Time to record a pixel: $t_p = 26\ \mu s$
- No. of cycles: $N_c = 48$

The combined HAADF-STEM/EDXS experiment was performed by using an electron beam with spot size 6 with a beam diameter $b_{beam} = 2.4 \pm 0.2$ Å and a similar (within ±3%) beam current density as given in Eq. (22).

In the following step, the region containing the NP selected for the thickness determination (orange frame in Fig. 4a), was divided into small elemental areas A_{elem} (schematically indicated by green frame in Fig. 5). The size of A_{elem} was chosen as a compromise between:

- the need for an as small as possible elemental area, which will assure a precise thickness determination reflecting every small detail of the NP shape. On the other hand, A_{elem} must be large enough to yield a reliable quantification of characteristic X-ray intensities on each EDX spectrum from A_{elem} with a suitable SNR value;
- a reasonably large number of processing data N_x and N_y along the x and y in-plane axes, which depend on the size of A_{elem}.

However, the main limitation of the A_{elem} size selection is related to the quantification of every EDX spectrum recorded from A_{elem} because choosing a too small A_{elem}, its corresponding EDX spectrum results in measured characteristic X-ray intensities of the chemical elements of interest with a poor precision characterized by a small *SNR* value.

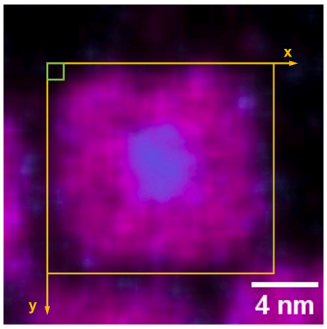


Fig. 5. Ca-Ce EDXS map of the single CeO_2-CaF_2 CS NP selected for the 3D shape reconstruction (orange dashed frame on Fig. 4a). The border of the reconstructed region together with the x- and y-directions are shown in orange, while a green frame schematically marks the small elemental area A_{elem}.

For the CS NP (Fig. 5), a good compromise between the size and reliable intensity quantification of every elemental EDX spectrum (EDX spectrum recorded by scanning the A_{elem}, which is the sum of the corresponding 36 individual EDX spectra recorded from each pixel inside A_{elem}) assuring a $SNR > 4$, was found for elemental areas formed by 6×6 pixels (green frame on Fig. 5) with a size of

$$A_{elem} = (6{\cdot}6){\cdot}a_p^2 = 20.794\ \text{Å}^2 \tag{46}$$

The selected elemental area of $A_{elem} = 20.794$ Å^2 leads to $N_x = 31$ along x and $N_y = 27$ along y (Fig. 5), resulting in a 3D-shape reconstruction performed for a total number of 837 points, which is reasonable for such a small particle.

3.2.2. *Data processing of 2D EDXS maps and 3D reconstruction of particle shape*

The thickness determination of the CeO_2-CaF_2 CS NP can be performed by using characteristic X-ray intensities of 1) either the Ce-L series or the O-K_α line or both of them for the CeO_2 region and of 2) either the Ca-K series or the F-K_α line or both of them for the CaF_2 region. Not only due to the large amount of data, which has to be processed for the thickness determination of this NP, but mainly due to difficulties related with the background simulation and subtraction for the low energy region of EDX spectra, resulting in larger errors of the measured intensities, the thickness determination of the NP will be based on the evaluation of the measured characteristic intensities of the Ce-L series for the core and of the Ca-K series for the shell.

The quantification of elemental EDX spectra recorded from each small A_{elem} along x- and y-directions results in two 2D matrices containing measured intensities for the characteristic Ca-K and Ce-L X-ray series $I_{i,j}^{Ca-K}$ *and* $I_{i,j}^{Ce-L}$ $(i = 1\ldots31$ *and* $j = 1\ldots27)$.

The quality of the measured intensities $I_{i,j}^{Ca-K}$ and $I_{i,j}^{Ce-L}$ is further evaluated by comparing their summation with the total acquired intensity of the Ca-K series and Ce-L series using the EDX spectrum recorded from the large orange frame (Fig. 5), $I_t^{Ca-K} = 4071$ $(counts)$ and $I_t^{Ce-L} = 428$ $(counts)$:

$$I_{sum}^{Ca-K} = \sum_i \sum_j I_{i,j}^{Ca-K} \textit{has to be equal to } I_t^{Ca-K} = 4071 \tag{47}$$

$$I_{sum}^{Ce-L} = \sum_i \sum_j I_{i,j}^{Ce-L} \textit{has to be equal to } I_t^{Ce-L} = 428 \tag{48}$$

The reason is that some elemental EDX spectra measured from small A_{elem}, could be noisy and by that the measured intensities of Ca-K and Ce-L series $I_{i,j}^{Ca-K}$ and $I_{i,j}^{Ce-L}$ can be affected by a poor SNR. However, for the NP under consideration, the intensity differences for the Ca-K and Ce-L series were < 5% supporting a rather good quality of the measured

intensities $I_{i,j}^{Ca-K}$ and $I_{i,j}^{Ce-L}$.

Elemental EDX spectra were recorded by using an electron beam with a diameter $b_{beam} = 2.4 \pm 0.3$ Å, which yields an illuminated surface $S_{beam} = 4.5239$ Å^2. To apply the theoretical calibration factors q_{Ca-K}^{calc} and q_{Ce-L}^{calc} for the thickness determination of the CeO_2-CaF_2 CS NP, every elemental EDX spectrum has to be normalized to an acquisition area with the size of S_{beam} and an acquisition time of 1 s.

Taking into account that each elemental EDX spectrum was recorded from a region with $A_{elem} = 20.7936$ Å^2 size (as indicated schematically by the green frame in Fig. 5), a surface correction factor *fact_s* has to be determined and applied to each experimental intensity $I_{i,j}^{Ca-K}$ and $I_{i,j}^{Ce-L}$ to account for the difference between the experimental acquisition area of A_{elem} and S_{beam}. This factor normalizes the acquisition surface A_{elem} to S_{beam}:

$$fact_s = \frac{S_{beam}}{A_{elem}} = 0.218 \tag{49}$$

Then, according to the experimental data, an elemental EDX spectrum was recorded for:

$$t_{exp} = (6{\cdot}6){\cdot}t_p{\cdot}N_c = (6{\cdot}6){\cdot}26{\cdot}10^{-6}{\cdot}48 = 4.493{\cdot}10^{-2}\ s \tag{50}$$

However, when each EDX spectrum recorded from S_{beam} would be acquired for 1 s, then an elemental EDX spectrum recorded from an area A_{elem} has to be acquired for a time interval:

$$t_{need} = \frac{A_{elem.}}{S_{beam}}{\cdot}1\ s = 4.596\ s \tag{51}$$

Accordingly, a time correction factor *fact_t* is needed for each experimental intensity $I_{i,j}^{Ca-K}$ and $I_{i,j}^{Ce-L}$ to account for the difference between the experimental t_{exp} and the necessary t_{need}, which will normalize the acquisition time of every EDX spectrum recorded from an area of S_{beam} to 1 s:

$$fact_t = \frac{t_{need}}{t_{exp}} = 102.306 \tag{52}$$

The surface- and time-corrected measured intensities of the Ca-K and Ce-L series can then be calculated as follows:

$$I_{corr\,i,j}^{Ca-K} = I_{i,j}^{Ca-K}{\cdot}fact_s{\cdot}fact_t \tag{53}$$

and

$$I_{corr\,i,j}^{Ce-L} = I_{i,j}^{Ce-L}{\cdot}fact_s{\cdot}fact_t \tag{54}$$

The calculation of the theoretical calibration factors of Ca-K and Ce-L series, i.e., q_{Ca-K}^{calc} and q_{Ce-L}^{calc}, is performed using Eq. (45) and the following considerations:

Crystalline CaF_2: crystalline *fcc* structure (Fm-3 m, space group No 225) with $n_{Ca} = 4$ Ca atoms within the unit cell with a lattice parameter of $a_{CaF2} = 5.4712$ Å and $V_{uc}^{CaF2} = 163.775$ Å^3;

- $M_{Ca} = 40.078\ u$ and $k_{Ca-K/Si} = 1.119$ from database in Ref. [25];
- $V_{beam}^{CaF2} = S_{beam}{\cdot}a_{CaF2} = 24.751$ Å^3

The theoretical calibration factor for the Ca-K series can then be calculated by using the experimental $w_{Pt-L}^{exp} = 4.441\ u/counts$ (Eq.(32)), $k_{Pt-L/Si} = 4.446$ from [25] with the same current densities as:

$$q_{Ca-K}^{calc} = \frac{V_{beam}^{CaF2}}{V_{uc}^{CaF2}}{\cdot}\frac{n_{Ca}{\cdot}M_{Ca}}{\left(w_{Pt-L}^{exp}{\cdot}\frac{k_{Ca-K/Si}}{k_{Pt-L/Si}}\right)} = 21.65\ counts\ for\ the\ path\ length\ a_{CaF2} \tag{55}$$

Crystalline CeO_2: crystalline *fcc* structure (Fm-3 m, space group No 225) with $n_{Ce} = 4$ Ce atoms within the unit cell with a lattice parameter of $a_{CeO2} = 5.4178$ Å and $V_{uc}^{CeO2} = 159.026$ Å^3;

- $M_{Ce} = 140.116\ u$ and $k_{Ce-L/Si} = 3.328$ from the database in [25];
- $V_{beam}^{CeO2} = S_{beam}{\cdot}a_{CeO2} = 24.510$ Å^3

The theoretical calibration factor of the Ce-L series can then be calculated as:

$$q_{Ce-L}^{calc} = \frac{V_{beam}^{CeO2}}{V_{uc}^{CeO2}}{\cdot}\frac{n_{Ce}{\cdot}M_{Ce}}{\left(k_{Pt-L}^{exp}{\cdot}\frac{k_{Ce-L/Si}}{k_{Pt-L/Si}}\right)} = 25.95\ counts\ for\ the\ path\ length\ a_{CeO2} \tag{56}$$

Using the values of theoretical calibration factors for the Ca-K and Ce-L series, matrices of path lengths $z_{i,j}^{Ca-K}(nm)$ and $z_{i,j}^{Ce-L}(nm)$ passed by the electron beam in the z-direction can be calculated at every point $\left(x_i, y_j\right)$ on the EDXS map by using the corrected measured intensities $I_{corr\,i,j}^{Ca-K}$ and $I_{corr\,i,j}^{Ce-L}$ and the following equations:

$$z_{i,j}^{Ca-K}(nm) = \frac{I_{corr\,i,j}^{Ca-K}}{q_{Ca-K}^{calc}}{\cdot}a_{CaF2}(nm) \tag{57}$$

$$z_{i,j}^{Ce-L} = \frac{I_{corr\,i,j}^{Ce-L}}{q_{Ce-L}^{calc}}{\cdot}a_{CeO2}(nm) \tag{58}$$

The matrices $z_{i,j}^{Ca-K}(nm)$ and $z_{i,j}^{Ce-L}(nm)$ allow to determine the sizes of Ca and Ce domains. The thickness map of the NP (Fig. 6a) is calculated using the $z_{i,j}^{t}(nm)$ matrix of the total path length passed through the NP by the electron beam in the z-direction, at every point $\left(x_i, y_j\right)$ on the EDXS map, given by:

$$z_{i,j}^{t}(nm) = z_{i,j}^{Ca-K}(nm) + z_{i,j}^{Ce-L}(nm) \tag{59}$$

To use the $z_{i,j}^{t}(nm)$ matrix for the 3D reconstruction of the NP shape, its convex, z-symmetrical shape has to be demonstrated for the symmetrical up-down reconstruction. Firstly, we note that the rectangular shape of the x-y projection of the NP chosen for the shape reconstruction (orange frame in the HAADF-STEM image in Fig. 4a) suggests its (rectangular) prismatic 3D symmetry. However, the tilt experiment presented in the following was used to further show the prismatic symmetry of CeO_2-CaF_2 CS NPs and to validate the 3D-shape reconstruction.

Within the tilt experiment, a given NP on the amorphous C-film surface initially without tilt (tilt 0°), is tilted by an angle α using the α-tilt function of the double-tilt sample holder. It is expected that a prismatic particle, which initially has no visible projection of its vertical facets on the HAADF-STEM image, will show visible projections of its facets after tilting by α. Knowing the projection length of its vertical facets $z_p(nm)$ and the tilting angle α°, the facet length $c_z(nm)$ (particle thickness) can be calculated according to (Fig. 7c):

$$c_z(nm) = \frac{z_p(nm)}{sin\ (\alpha^{\circ})} \tag{60}$$

Unfortunately, the tilt experiment could not be applied to validate the prismatic 3D symmetry of the NP used for the 3D-shape reconstruction (orange frame in Fig. 4a), because after tilting the projections of its vertical facets were not sharp enough to be visualized and reliably evaluated. Instead, another CeO_2-CaF_2 CS NP with a favorable orientation on the same sample was selected (Fig. 7), assuming that all NPs prepared in the same synthesis experiment under equilibrium conditions are statistically similar and have the same morphology. This assumption is supported by considering their overview HAADF-STEM images, which show the formation of NPs with a narrow size distribution and rectangular 2D-projected shapes with sizes of $10.8 \pm 5.2\ nm$ and $12.0 \pm 2.4\ nm$ for the short and long edges, respectively [30]. Accordingly,

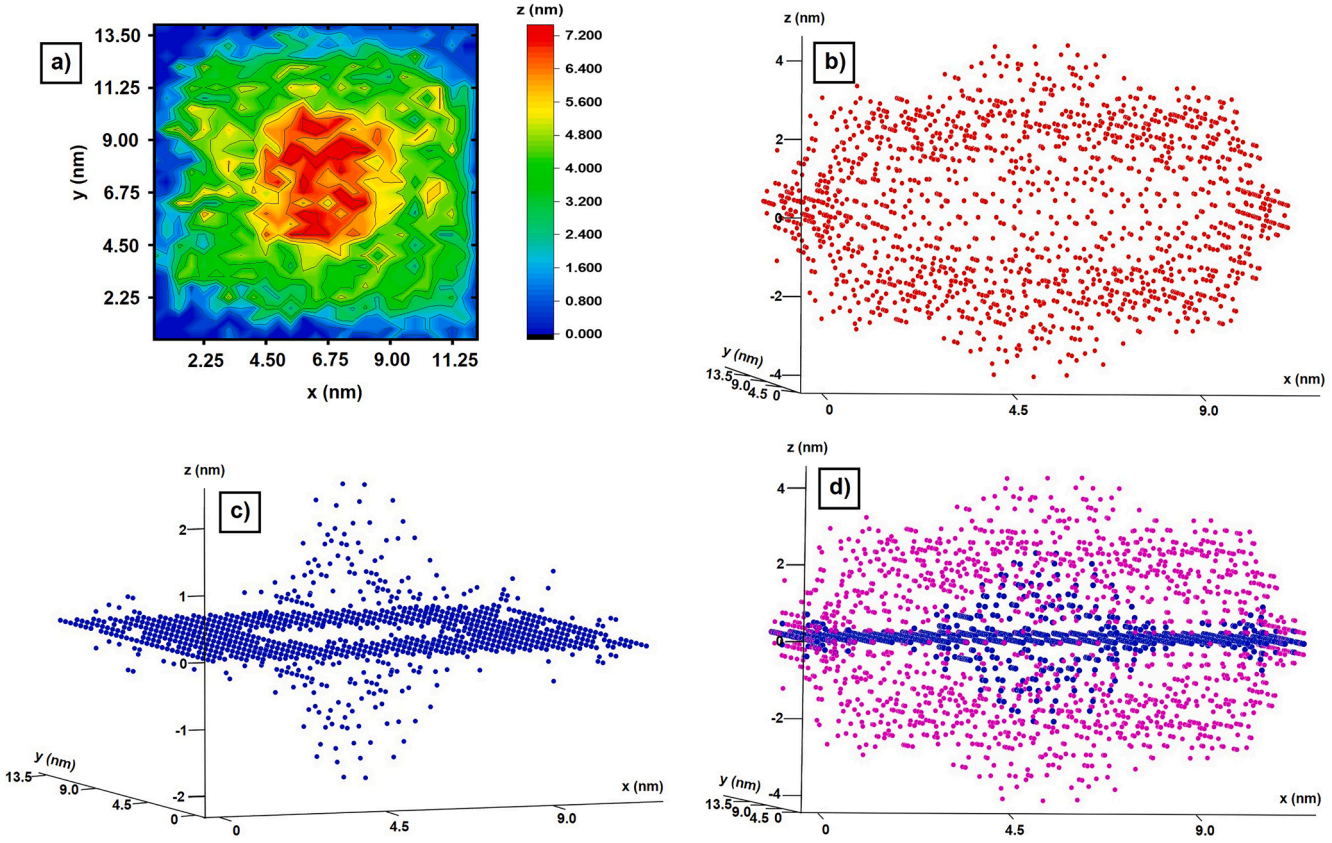


Fig. 6. a) Thickness map of the CeO_2-CaF_2 CS NP in Fig. 5 calculated using its $z^t_{i,j}(nm)$ matrix; b) 3D shape reconstruction of the CS NP by using the $z^t_{i,j}(nm)$ and Eq. (61) (red symbols); c) 3D reconstruction of the CeO_2 core shape only by using the $z^{Ce-L}_{i,j}(nm)$ matrix and Eq. (61) (blue symbols); d) 3D shape reconstruction of the CaF_2 shell only from $z^{Ca-K}_{i,j}(nm)$ matrix and Eq. (62) with $\Delta z = 0\ nm$; here, the 3D core shape forms its inner surface (blue symbols) and 3D particle shape its outer surface (pink symbols). Blue points on the $z = 0$ plane are a drawing artifact that do not represent the 3D reconstructed shapes.

HAADF-STEM images of a selected NP before (Fig. 7a) and after tilting (Fig. 7b) will be used in the following not only to demonstrate its prismatic (convex) 3D symmetry, but also to determine the NP thickness and the z-location of the core center relative to the center of the entire NP, information necessary for the 3D reconstruction of the NP-shell shape.

Fig. 7a shows the HAADF-STEM image of the selected NP at 0° tilt, which has a rectangular 2D-projected shape with lateral sizes of $a_x \approx 17\ nm$ and $b_y \approx 15\ nm$. The HAADF-STEM image of NP recorded after tilting by $\alpha = 20°$ shows a prismatic projected shape with the (projected) length of its vertical facet of $z_p = 2.1 - 2.4\ nm$ (Fig. 7b). Using the z_p value, vertical facets with a thickness of $c_z = 6.2 - 7.0\ nm$ can be calculated by applying Eq. (60), which confirms the formation of particles with a prismatic 3D symmetry in this synthesis, characterized by $c_z < b_y \approx a_x$ and allows to apply the reconstruction method to obtain their 3D shape.

Using the $z^t_{i,j}(nm)$ matrix given by Eq. (59), the 3D z-symmetric reconstruction of the NP shape can be performed by defining two matrices $z^{up}_{i,j}(nm)$ and $z^{bottom}_{i,j}(nm)$ according to:

$$z^{up}_{i,j}(nm) = \frac{z^t_{i,j}(nm)}{2} \ \text{and}\ z^{bottom}_{i,j}(nm) = -\frac{z^t_{i,j}(nm)}{2} \tag{61}$$

The two matrices are plotted in Fig. 6b, each of them representing the 3D shape of a half of the NP (red dots at every point (x_i, y_j)). Based on the 3D-shape reconstruction, the CeO_2-CaF_2 CS NP (Fig. 6a,b) has a prismatic lens shape characterized by horizontal square facets with lengths of $a_x \cong b_y = 12\ nm$, similar to those measured on the HAADF-STEM image (Fig. 4a), and a thickness of $c_z \cong 5 - 6\ nm$ with a maximal thickness of $c_z \cong 7 - 8\ nm$ in the center (Fig. 6a). Such a typical geometry of NP characterized by $c_z < a_x \approx b_y$ agrees with that found by tilt experiments also for other NPs synthetized within the same experiment. Regarding the drawing, we note that the 3D-shape reconstruction is defined by only (x_i, y_j) points with $z_{i,j}(nm) \neq 0$. However, because the image is obtained by plotting $z_{i,j}(nm)$ matrices, points (x_i, y_j), which do not belong to the reconstructed object, will become $z_{i,j}(nm) = 0$ values and will be shown on the reconstructed image in the $z = 0$ plane (visible as blue dots in Fig. 7c,d). This is only a drawing artifact that artificially extends the 3D-reconstructed shapes over the whole investigated region (x_i, y_j) with $i = 1...31$ *and* $j = 1...27$ and do not represent the 3D-reconstructed shapes.

While the $z^t_{i,j}(nm)$ matrix and Eq. (61) describes the 3D shape of the whole particle, matrices $z^{Ca-K}_{i,j}(nm)$ and $z^{Ce-L}_{i,j}(nm)$ can be used to visualize the 3D shape of the core and the shell only. Taking into account that the 3D-shape reconstruction is z-symmetrically performed, the shape reconstruction of its constituents has to start from the particle interior, i.e., from the Ce core. The 3D-shape reconstruction of the NP core and shell, can benefit from additional information about their chemical composition. This can be obtained by the analysis of Ca- and Ce-concentration profiles obtained after the quantification of an EDXS line scan that passes through the NP center in the x-direction. The EDXS line profile is evaluated by applying the subshell approach developed for CS NPs with a cubic shell – spherical core [31]. Within our experimental resolution of 1 nm, it indicates the formation of CS NPs with a pure CaF_2 shell and pure CeO_2 core.

Considering the formation of a pure CeO_2 core as indicated by the EDXS line scan analysis, the 3D-reconstruction method performed by

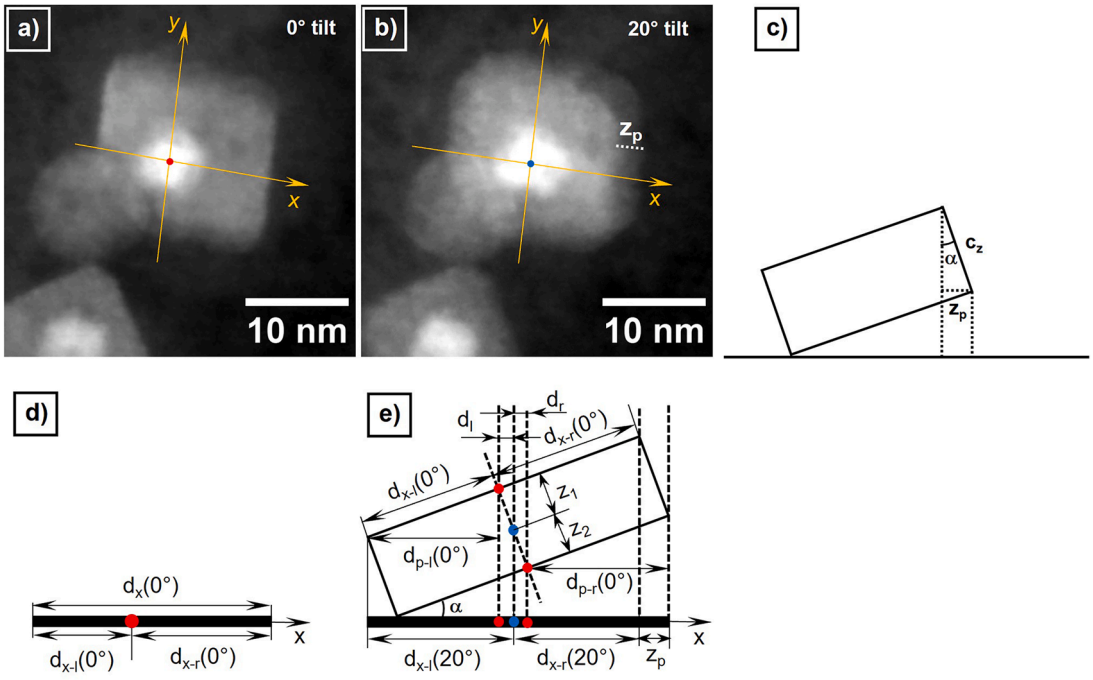


Fig. 7. Tilt experiment of a CeO_2-CaF_2 CS NP: a) HAADF-STEM image of the NP at 0° tilt, where a red dot marks the position of the core center and b) after tilting by 20°, where a vertical facet with a projection length z_p becomes visible in the HAADF-STEM image; a blue dot marks the core center position; c) the schematic drawing shows the geometrical considerations used to calculate the length of the vertical facet c_z with a projection distance z_p after tilting by $\alpha = 20°$; d)-e) schemes of the NP dimensions (d) at 0° tilt and (e) at 20° tilt used to calculate the z-position of the NP-core center relative to the z-location of the NP center; two red dots in (e) located on the upper/bottom NP surfaces mark the core center position before tilting.

using the $z_{i,j}^{Ce-L}(nm)$ matrix and Eq. (61) can get the 3D shape of the core only, when the core itself has a convex, z-symmetrical shape. Unfortunately, the tilt experiment does not clearly demonstrate the convex NP-core shape, because both HAADF-STEM images in Fig. 7a,b show a diffuse contrast of the core region. However, reliable information about the core shape can be obtained by considering the synthesis procedure of these CS NPs [30]. According to that, the CeO_2 cores are first synthesized, resulting in the formation of NPs with sizes of $7.4 \pm 3.4\ nm$ and a convex, regular polyhedral (truncated octahedral) shape [30]. Then, these cores are used as starting seeds for growing the CaF_2-NP shell. Using the contrast difference between core and shell domains on the HAADF-STEM images, the approximate size of the core region was statistically determined to be only slightly smaller of $6.7 \pm 3.4\ nm$ compared to the size of the starting seeds [30]. This supports the assumption of a small alteration of the cores during shell growth. Accordingly, it is reasonable to assume that the CeO_2 cores preserve their convex, 3D-symmetric polyhedral shape after shell growth [30] and allows the 3D reconstruction of the CeO_2 core shape by using the $z_{i,j}^{Ce-L}(nm)$ matrix and Eq. (61) (Fig. 6c).

The 3D-shape reconstruction of the CaF_2 shell will be further obtained by putting the Ca distribution described by the $z_{i,j}^{Ca-K}(nm)$ on top of the Ce distribution represented by $z_{i,j}^{Ce-L}(nm)$ matrix, taking into account that the outer shell surface has to coincide with the external NP surface. However, for getting a reliable 3D reconstruction of the shell shape, the core has to be located at the right z-position within the NP. For that, the z-position of the x-y symmetry plane of the core (the core center) relative to that of the entire NP (particle center) has to be determined. Generally, when the core center is located at a distance $z_1(nm)/z_2(nm)$ from the upper/bottom particle surface along to the z-axis and the center of the entire NP at the distance of $z_0(nm) = \frac{c_z}{2}$, the 3D-reconstructed shape of the shell distribution (i.e. the Ca distribution) can be defined by its outer (up and bottom) and inner (up and bottom) surfaces calculated according to the following relations:

$$\begin{cases} z_{i,j}^{Ca-K\ outer\ up}(nm) = \dfrac{z_{i,j}^{Ca-K} + z_{i,j}^{Ce-L}}{2} = \dfrac{z_{i,j}^{t}(nm)}{2} \\ z_{i,j}^{Ca-K\ outer\ bottom}(nm) = -\dfrac{z_{i,j}^{t}(nm)}{2} \\ z_{i,j}^{Ca-K\ inner\ up}(nm) = \dfrac{z_{i,j}^{Ce-L}(nm)}{2} + \Delta z\ \ and \\ z_{i,j}^{Ca-K\ inner\ bottom}(nm) = -\dfrac{z_{i,j}^{Ce-L}(nm)}{2} + \Delta z \end{cases} \quad (62)$$

where $\Delta z = z_0 - z_1$ has to be determined, which describes the shift of the core center along z relative to the center of the entire NP.

The tilt experiment shown in Fig. 7 can be used to calculate $z_1(nm)$ and $z_2(nm)$, which are distances along the z-axis between the core center and the upper (z_1) and the bottom NP surface (z_2), respectively (scheme in Fig. 7e). The red/blue dots in Fig. 7a/b represent the core center of the NP within the x-y plane of the HAADF-STEM image at 0° and 20° tilt. Due to the diffuse core contrast, the x- and y-positions of these points are determined in the middle of the region with a bright contrast (core) of two intensity line profiles along the x- and y-directions through the core (Fig. 7a,b). In the HAADF-STEM image Fig. 7a (NP at 0° tilt) $d_{x-l}(0°) = 7.2 \pm 0.5\ nm$ and $d_{x-r}(0°) = 9.9 \pm 0.5\ nm$ are measured, representing distances measured from the left/right NP edge to the core center (see notations in Fig. 7d). For the NP under tilted conditions (20° tilt), $d_{x-l}(20°) = 7.8 \pm 0.5\ nm$ and $d_{x-r}(20°) = 8.1 \pm 0.5\ nm$ are measured in Fig. 7b (see notations in Fig. 7e). In the tilted position (Fig. 7b), projected lengths of $d_{p-l}(0°) = d_{x-l}(0°) \cdot \cos(20°) = 6.8\ nm$, $d_{p-r}(0°) = d_{x-r}(0°) \cdot \cos(20°) = 9.3\ nm$ and $d'_{p-r}(0°) = d_{p-r}(0°) - z_p = 7.2\ nm$ are calculated, taking into account that the two red points are the z-positions above/below the core center of the upper/bottom NP surface without tilt (see notations in Fig. 7e). This yields distances of $d_l = d_{x-l}(20°) - d_{p-l}(0°) = 1.0\ nm$ and $d_r = d_{x-r}(20°) - d'_{p-r}(0°) = 0.9\ nm$ (notations in Fig. 7e). Finally, $z_1 = \frac{d_l(nm)}{\sin(20°)} = 3.1 \pm 0.5\ nm$ and $z_2 =$

$\frac{d_r(nm)}{\sin(20^\circ)} = 2.7 \pm 0.5$ *nm* (notations in Fig. 7e) are calculated, which has to be compared with $z_0 = \frac{c_z(nm)}{2} = 3.1 \pm 0.3$ *nm* to determine the z-position of the core center relative to that of the entire NP. Firstly, we note that $c_z \cong z_1 + z_2 \cong 6.0$ *nm* (within the error bars) proving the validity and precision of these calculations. Secondly, we observe that, despite an acentric core location within the x-y plane of the HAADF-STEM image without tilt (Fig. 7a), values of $z_1 \cong z_2 \cong z_0 = 3.1$ *nm* result in $\Delta z = 0$ *nm* within error bars, i.e., the core center is located at the same z-position as the center of the entire NP. The same location of the NP core in the center of the entire NP is obtained after the evaluation of tilt experiments for two other CeO_2-CaF_2 CS NPs (not shown in the manuscript). Assuming the synthesis of similar NPs characterized by similar parameters, it can be considered highly probable that most NPs in the sample, also the NP used for the 3D reconstruction, are characterized by $\Delta z = 0$ *nm*.

Then, the 3D reconstruction of the CaF_2 shell can then be performed by using Eq. (62) with $\Delta z = 0$ *nm* and is described by an inner surface, represented by the 3D-shape reconstruction of the pure Ce core based on the $z_{i,j}^{Ce-L}(nm)$ matrix (blue symbols in Fig. 6d), while its outer surface is represented by the 3D shape of entire particle (pink symbols in Fig. 6d).

3.3. Thickness and 3D-shape reconstruction of an $Au_{35}Co_{65}$ core-shell nanoparticle

The same procedure is applied to obtain the thickness and 3D shape of an alloyed Au-Co CS NP with the average chemical composition $Au_{35\pm3}Co_{65\pm4}$ experimentally determined by the quantification of its EDXS maps (orange frame in Fig. 8d). The experimental parameters used to record the elemental EDXS maps for the 3D reconstruction of the NP shape are:

- Pixel size: $a_p = 0.54$ Å
- Time to record a pixel: $t_p = 20$ *μs*
- No. of cycles: $N_c = 28$

The HAADF-STEM/EDXS experiment was performed by using the convergent electron beam with a beam diameter of $b = 2.5 \pm 0.3$ Å and a similar (within ±2%) beam current density as given in Eq. (22), which yields an illuminated surface $S_{beam} = 4.909$ Å^2. For the CS NP selected for the thickness determination (Fig. 8a), elemental areas formed by 19×19 pixels (schematically indicated by the green frame in Fig. 8d) with $A_{elem} = 105.268$ Å^2 were found to be suitable. The selected A_{elem} yields $N_x = 38$ along x and $N_y = 39$ along y (Fig. 8d), resulting in a thickness determination performed with a total number of 1482 points. The thickness determination of the $Au_{35}Co_{65}$ CS NP was performed by using the characteristic X-ray intensities of the Au-L and Co-K series.

The quantification of the elemental EDX spectra yields two 2D matrices containing measured intensities of the Au-L and Co-K X-ray series $I_{i,j}^{Au-L}$ *and* $I_{i,j}^{Co-K}$ ($i = 1...38$ *and* $j = 1...39$). The summation of $I_{i,j}^{Au-L}$ and $I_{i,j}^{Co-K}$ and the total measured intensity of the Au-L and Co-K series of the EDX spectrum recorded from the large orange frame (Fig. 8d), $I_t^{Au-L} = 315885$ *counts* and $I_t^{Co-K} = 366462$ *counts*, are in good agreement with differences for the Au-L and Co-K series < 5% supporting a good quality of the measured intensities $I_{i,j}^{Co-K}$ and $I_{i,j}^{Au-L}$.

A surface correction factor of $fact_s = 4.66 \cdot 10^{-2}$ can be calculated replacing $S_{beam} = 4.909$ Å^2 and $A_{elem} = 105.268$ Å^2 in Eq. (49). From the experimental set-up of the 2D EDXS map acquisition, an experimental measuring time of $t_{exp} = (19 \cdot 19) \cdot 20 \cdot 10^{-6} \cdot 28 = 0.2022$ *s* and a needed time of $t_{need} = 21.445$ *s* is calculated, which are replaced in Eq. (52) and yield a time correction factor $fact_t = 106.058$. These two correction factors, *fact_s* and *fact_t*, are further used to determine the corrected intensities $I_{corr\,i,j}^{Au-L}$ and $I_{corr\,i,j}^{Co-K}$ according to Eqs. (53)/(54).

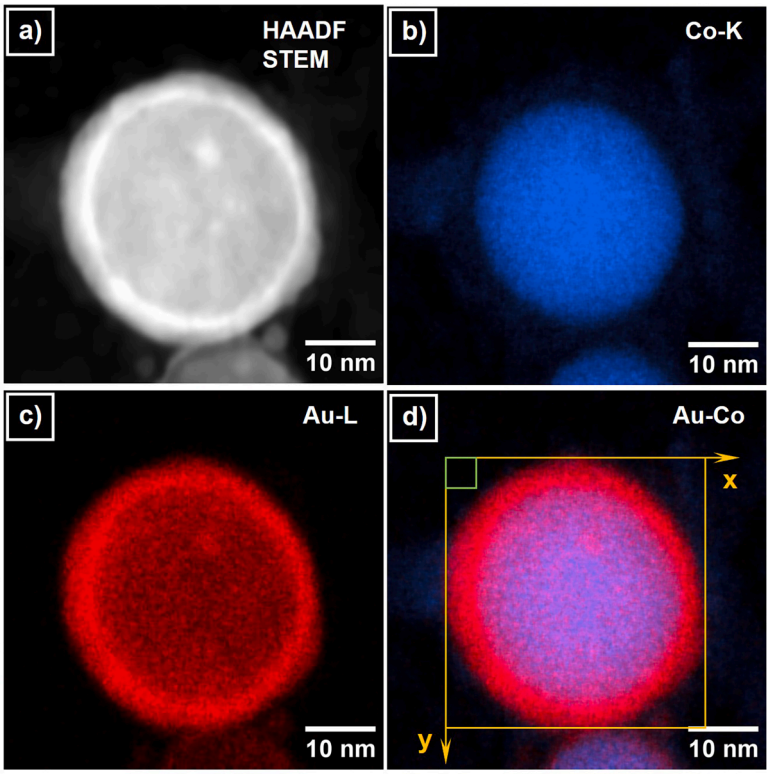


Fig. 8. $Au_{35}Co_{65}$ CS NP: a) HAADF-STEM image and (b)-(d) corresponding elemental EDXS maps of (b) Co (Co-K series, blue), (c) Au (Au-L series, red) and (d) superposition of the Au and Co maps together with the border of the 3D reconstruction region with the x- and y-directions shown in orange and the green frame schematically marking the A_{elem}.

The calculation of theoretical calibration factors of Au-L and Co-K series q^{calc}_{Au-L} and q^{calc}_{Co-K} is performed using Eq. (45) and the following considerations:

Crystalline Au: crystalline *fcc* structure (Fm-3 m, No 225) with $n_{Au} = 4$ Au atoms within the unit cell with a lattice parameter of $a_{Au} = 4.078$ Å and $V^{Au}_{uc} = 67.828$ Å^3;

- $M_{Au} = 196.96655\ u$ and $k_{Au-L/Si} = 4.558$ from database in [25];
- $V^{Au}_{beam} = S_{beam} \cdot a_{Au} = 20.019$ Å^3

Accordingly, a calculated calibration factor for the Au-L series of $q^{calc}_{Au-L} = 51.02\ counts$ for the path length a_{Au} is obtained.

Crystalline Co: crystalline *hcp* structure ($P6_3/mmc$, No 194) with $n_{Co} = 2$ Co atoms within the unit cell, characterized by lattice parameters of $a_{Co} = 2.514$ Å and $c_{Co} = 4.105$ Å, angles of $\alpha = \beta = 90°$ *and* $\gamma = 120°$, and a volume of $V^{Co}_{uc} = 22.47$ Å^3;

- $M_{Co} = 58.9332\ u$ and $k_{Co-K/Si} = 1.564$ from database in [25];
- $V^{Co}_{beam} = S_{beam} \cdot c_{Co} = 20.150$ Å^3

A theoretical calibration factor for the Co-K series of $q^{calc}_{Co-K} = 67.58\ counts$ can be determined for the path length c_{Co}. The particular orientation of the hexagonal unit cell with c_{Co}, which is perpendicular on the x-y surface of the unit cell, along the electron-beam direction z, is chosen just for simplicity and plays no role in the calculation of the $z^{Co-K}_{i,j}(nm)$ matrix

$$z^{Co-K}_{i,j}(nm) = \frac{I^{Co-K}_{corr\,i,j}}{q^{calc}_{Co-K}} \cdot c_{Co}(nm) = \frac{I^{Co-K}_{corr\,i,j} \cdot \left(w^{exp}_{Pt-L} \cdot \frac{k_{Co-K/Si}}{k_{Pt-L/Si}} \right) \cdot V^{Co}_{uc}}{S_{beam} \cdot n_{Co} \cdot M_{Co}} \quad (63)$$

Eq. (63) shows that $z^{Co-K}_{i,j}(nm)$ values do not explicitly depend on the c_{Co} path length, but on V^{Co}_{uc} and then, every orientation of the unit cell yields the same $z^{Co-K}_{i,j}(nm)$ values.

Using the values for the calculated calibration factors of the Au-L and Co-K series, matrices of path lengths $z^{Co-K}_{i,j}(nm)$ and $z^{Au-L}_{i,j}(nm)$ through the NP can be calculated at every point (x_i, y_j) on the EDXS map by using Eq. (57)/(58). Finally, the matrix $z^{t}_{i,j}(nm)$ of the total path length through the particle along the z-direction determined according to Eq. (59) yields its thickness map (Fig. 9a).

The convex, z-symmetrical NP shape has to be demonstrated before the application of the 3D-reconstruction method based on the matrix $z^{t}_{i,j}(nm)$ and Eq. (61). Firstly, we note the elliptical shape of the x-y projection of CS NP (HAADF-STEM image in Fig. 8d). In addition, a tilt experiment similar to that presented in Chap. 3.2.2. is performed to show the ellipsoidal 3D symmetry of the Au-Co CS NP (for details see **Chap. S1.** in the ESI). The elliptical 2D projection of this NP at 20° tilt (HAADF-STEM image in Fig. S1b) demonstrates its ellipsoidal 3D-symmetry and validates the use of the z-symmetric reconstruction method. Accordingly, its 3D-shape reconstruction was performed using the matrix $z^{t}_{i,j}(nm)$ of the total path length through the NP along the z-direction and Eq. (61), which yields an ellipsoidal NP shape (Fig. 9b). The (ellipsoidal) shape is characterized by x-y diameters $d_x \cong 38\ nm$ and $d_y = 39\ nm$, similar to those measured in HAADF-STEM images (Fig. 8a and Fig. S1a) and a size of about $d_z \cong 31 - 32\ nm$ along the z-direction (Fig. 9a and b).

While $z^{t}_{i,j}(nm)$ give the 3D shape of the entire NP, the $z^{Co-K}_{i,j}(nm)$ and $z^{Au-L}_{i,j}(nm)$ matrices can be used to gain information about the 3D shape of the core and the shell only. Beneficial for that could be additional information about their chemical compositions obtained by the analysis of the Au- and Co-composition profiles determined after the quantification of an EDXS line scan passing through the NP center and further evaluated by applying the subshell approach developed for CS NPs with an elliptical shell and core [32]. It shows that the $Au_{35}Co_{65}$ CS NP consists of an alloyed shell with the average chemical composition of $Au_{66\pm3}Co_{34\pm3}$ and thicknesses of $t \cong 3 - 4\ nm$ and a pure Co core with a diameter of $d_{x-y} \cong 30 - 32\ nm$ along the EDXS line scan direction in the x-y plane. Due to the formation of an Au-Co alloyed shell, the 3D-shape reconstruction of the core and the shell based on the $z^{Co-K}_{i,j}(nm)$ or $z^{Au-L}_{i,j}(nm)$ elemental matrices, as shown in the case of the CeO_2-CaF_2 CS NP, is not possible anymore, because the "delocalization" of the EDXS signal along the electron-beam direction z, does not allow the direct identification of the position from which a Co or Au X-ray signal is generated in the NP.

However, the combination between the 3D-shape reconstruction of the Co and Au distributions based on $z^{Co-K}_{i,j}(nm)$ and $z^{Au-L}_{i,j}(nm)$ matrices and Eq. (61) (Fig. 10a and c) and the 2D EDXS elemental maps of Au-L and Co-K (Fig. 8b and c) can overcome the signal delocalization and allows to obtain realistic shapes for the core and the shell only. The z-symmetric 3D-shape reconstruction of particle constituents, like the core and the shell of CS NPs, has to start from the particle interior, i.e., from the Co core in our case. The 2D EDXS map of Co-K shows a bright Co signal in the particle inner with a slightly elliptical shape and diameters of $d_x \cong 30\ nm$, $d_y \cong 32\ nm$, and an about $t_{x,y} \approx 3 - 4\ nm$ thick ring

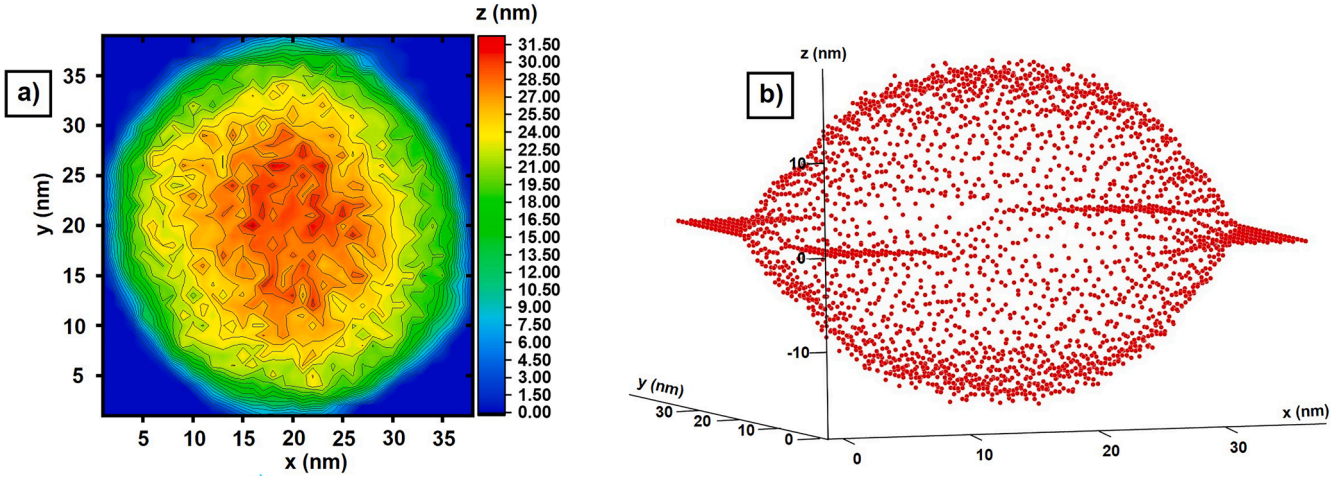


Fig. 9. a) Thickness map of the $Au_{35}Co_{65}$ CS NP calculated by using its $z^{t}_{i,j}(nm)$ matrix; b) 3D shape reconstruction of the CS NP using the $z^{t}_{i,j}(nm)$ matrix and Eq. (61) (red symbols). Points on the $z = 0$ plane are a drawing artifact that do not represent the 3D reconstructed shape.

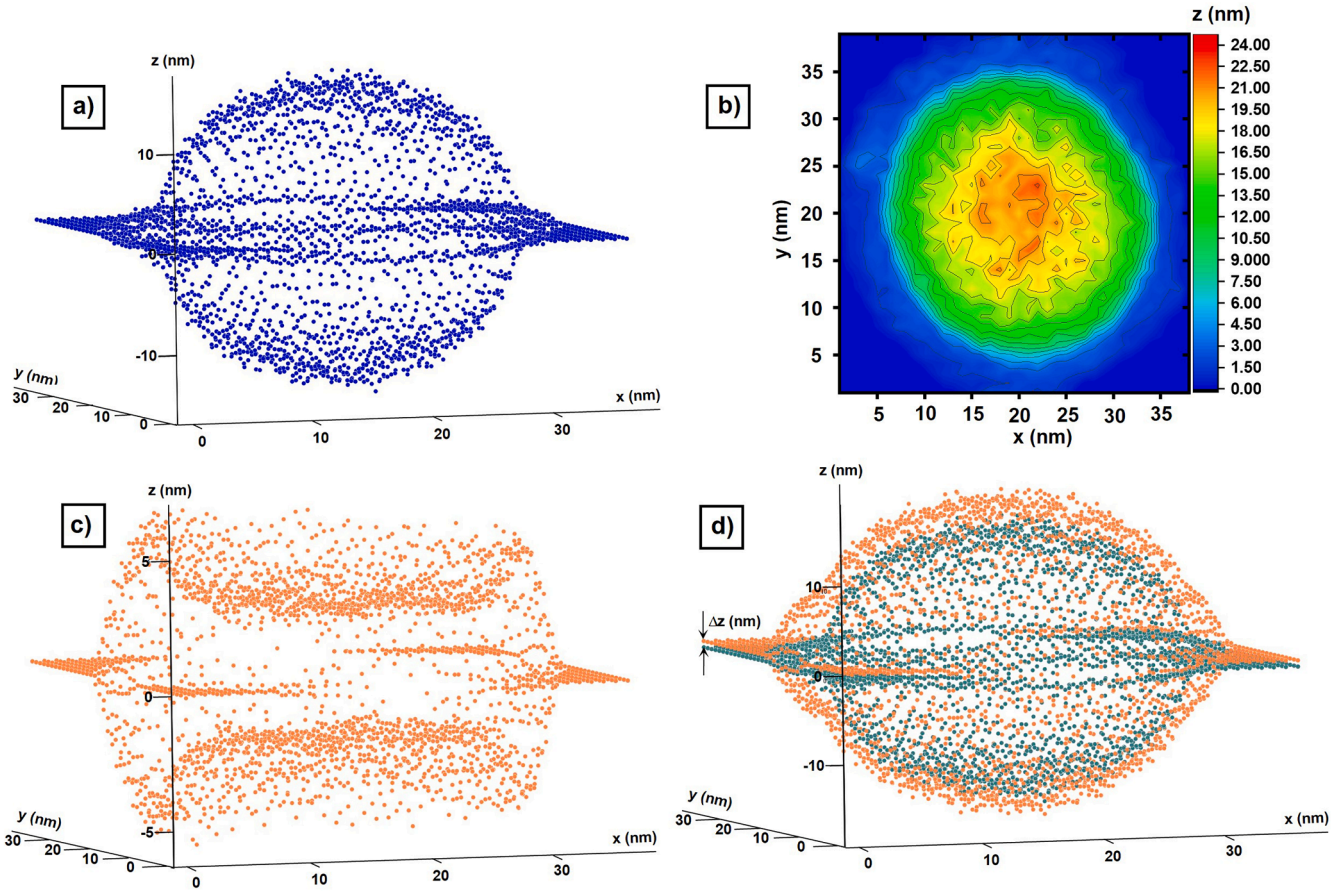


Fig. 10. a) 3D shape reconstruction of the Co distribution based on the $z_{i,j}^{Co-K}(nm)$ matrix and Eq. (61) (blue symbols); b) thickness map of the Co distribution in a); c) 3D shape reconstruction of the Au distribution based on the $z_{i,j}^{Au-L}(nm)$ matrix and Eq. (61) (orange symbols); d) real 3D shape reconstruction of the Au distribution based on the $z_{i,j}^{Au-L}(nm)$ matrix and Eq. (62), where its outer surface is described by the $z_{i,j}^{t}(nm)$ matrix (orange symbols) and its inner surface by the 3D distribution of Co (green symbols) shifted down by $\Delta z = -0.7\ nm$ according to the tilt experiment. Points on the $z = 0$ and $z = -0.7\ nm$ planes are a drawing artifact that do not represent the 3D reconstructed shapes.

outside with a much weaker Co signal (Fig. 8b). The 3D-shape reconstruction of the Co distribution determined from the $z_{i,j}^{Co-K}(nm)$ matrix and Eq. (61) (Fig. 10a) and its corresponding thickness map calculated using the $z_{i,j}^{Co-K}(nm)$ matrix (Fig. 10b) results in a x-y projection with an elliptical shape and diameters of $d_x \cong 30\ nm, d_y \cong 32\ nm$ and an external ring outside with a thickness of $t_x \approx t_y = 3 - 4\ nm$, in agreement to the EDXS map (Fig. 8b). However, in the x-z/y-z projection the distribution shows an elliptical shape with a diameter of $d_z \cong 25 - 26\ nm$ with two rounded extensions in the middle with thicknesses of up to $t_z \leq 2 - 3\ nm$ (clearly visible on the right and left side of Fig. 10a and on the thickness map on Fig. 10b). On the other side, the EDXS map of Au-L shows a bright red ring with a thickness of $t_x \approx t_y = 3 - 4\ nm$ at the NP surface and a dark red signal in the particle inner (Fig. 8c), while the 3D-shape distribution of Au calculated by replacing in Eq. (61) the $z_{i,j}^{Au-L}(nm)$ matrix, results in two concave regions in the particle inner, which are unrealistic (Fig. 10c). Because the outer shell surface has to coincide with the external NP surface, the real 3D-shape reconstruction of the Au distribution will be obtained by putting the Au distribution described by the $z_{i,j}^{Au-L}(nm)$ on top of the Co distribution represented by $z_{i,j}^{Co-K}(nm)$ matrix and replacing them in Eq. (62). For the visualization of the 3D-shape reconstruction can be considered that $z_{i,j}^{Co-K}(nm)$ forms the inner surface of the Au distribution, while the outer surface of Au distribution is represented by the external surface of the entire particle (Fig. 10d). Similar with the 3D-shape reconstruction of the Ca shell, the 3D shape of the Au distribution is defined by its outer (up and bottom) and inner (up and bottom) surfaces, which are calculated according to Eq. (62) by using $\Delta z = -0.7\ nm$ determined from the tilt experiment (details in **Chap. S1** in the ESI).

The application of the 3D-reconstruction method to get the Co-core shape is allowed if the core itself has a convex, z-symmetrical shape. The elliptical x-y core projection in the HAADF-STEM image (Fig. 8a) supports an ellipsoidal 3D-symmetric core. Moreover, the HAADF-STEM image of the tilted NP in Fig. S1b shows an elliptical x-y projection of the tilted core, suggesting an ellipsoidal 3D-symmetric CS NP core, which facilitates the use of the 3D-reconstruction method.

Due to the formation of an alloyed Au-Co shell, the 3D-shape reconstruction of the Co-distribution performed by using the $z_{i,j}^{Co-K}(nm)$ matrix and Eq. (61) (Fig. 10a) will not represent the core shape anymore. In this case, the 3D reconstruction of the core has to be performed by using the $I_{i,j}^{Co-K-core}$ matrix of the measured intensities of Co-K series recorded from the core only, which is calculated by separating in the $I_{i,j}^{Co-K}$ matrix the Co contribution of the shell from that of the core, based on some considerations. Firstly, the outer NP borders in the x-y plane will be defined by using the $z_{i,j}^{t}(nm)$ matrix. Important are the indices of the left-down (i_l, j_d), left-up (i_l, j_u), right-down (i_r, j_d) and right-up (i_r, j_u) NP edges. In a second step, all measured Co-intensity values $I_{m,n}^{Co-K} \neq 0$ of the $I_{i,j}^{Co-K}$ matrix located in the shell region, i.e., up to a thickness $t_{shell} \cong 3 - 4\ nm$ from the corresponding outer edges in

the x-y plane, and defined by $(i_l \le m \le (i_l+4), j_d \le n \le j_u)$, $(i_l \le m \le i_r, j_d \le n \le (j_d+3))$, $((i_r-3) \le m \le i_r, j_d \le n \le j_u)$ and $(i_l \le m \le i_r, (j_u-4) \le n \le j_u)$ will be normalized to a thickness of $2{\cdot}t_z \cong 7\ nm$, by using their corresponding total thickness matrix elements $z^t_{m,n}(nm)$ according to:

$$I^{Co-K}_{m,n}(norm) = \frac{I^{Co-K}_{m,n}\cdot 7\ nm}{z^t_{m,n}(nm)} \tag{64}$$

This procedure is based on the fact that along the z-axis of the NP, the electron beam passes twice through the shell with a measured in-plane x-y thickness of $t^{shell}_{x-y} \cong 6-7\ nm$ and by taking into account that the distance between two successive points in the $I^{Co-K}_{i,j}$ matrix along the x- and y-directions is $\Delta i = \Delta j = 19{\cdot}a_p = 1.026\ nm$. The normalization is necessary because points within the NP shell with $z^t_{m,n}(nm) < 7\ nm$ will have $I^{Co-K}_{m,n}$ values smaller than the I^{Co-K} value corresponding to 7 nm. Then, the average value $I^{Co-K-shell}$ is calculated as:

$$I^{Co-K-shell} = \frac{\sum_{m,n} I^{Co-K}_{m,n}(norm)}{\sum_{m,n} 1} \tag{65}$$

Assuming the formation of a chemically homogeneous Au-Co shell with a thickness of $t_z = 7\ nm$, the $I^{Co-K-core}_{i,j}$ matrix of the measured intensity of Co-K series from only the core can be calculated as the difference

$$I^{Co-K-core}_{i,j} = I^{Co-K}_{i,j} - I^{Co-K-shell} \tag{66}$$

Here, all $I^{Co-K-core}_{i,j} \le 0$ will be set to $I^{Co-K-core}_{i,j} = 0$, taking into account that $I^{Co-K}_{i,j} \le I^{Co-K-shell}_{i,j}$ at (m,n)-positions within the 3–4 nm shell thickness or outside the NP edges characterized by $z^t_{m,n}(nm) < 7\ nm$. In a procedure similar to that described above, $I_{corr}{}^{Co-K-core}_{i,j}$ is calculated using *fact_s* and *fact_t* values and Eq. (53)/(54). The matrix $z^{Co-K-core}_{i,j}(nm)$ can then be determined by inserting q^{calc}_{Co-K} in Eq. (57) and yields the thickness map of the Co core (Fig. 11a). Furthermore, $z^{Co-K-core}_{i,j}(nm)$ matrix and Eq. (61) was used to visualize the 3D-shape reconstruction of the pure Co-core shape only (Fig. 11b). It indicates the formation of an ellipsoidal Co core with diameters of $d^{core}_x \cong 29\ nm$ and $d^{core}_y \cong 31\ nm$ in the x-y image plane and $d^{core}_z \approx 22-23\ nm$ in z-direction (Fig. 11a and b) in agreement with the assumption of an ellipsoidal NP core formation.

However, for the use of the $z^{Co-K-core}_{i,j}(nm)$ matrix and Eq. (62) to reconstruct the 3D shape of the shell, the z-position of the core center relative to the center of the entire NP was determined by geometrical evaluations of the CS NP at 0° and 20° tilt (see Chap. S1. in the ESI). A downshift of the core center by $\Delta z \cong -0.7\ nm$ is obtained with respect to the center of the entire NP. The 3D-shape reconstruction of the Au shell is then defined by its outer surface represented by the external surface of the entire NP and calculated using the first two relations of Eq. (62). Its inner surface is determined by replacing in the last two relations of Eq. (62) the $z^{Co-K-core}_{i,j}(nm)$ matrix and taking $\Delta z = -0.7\ nm$ (Fig. 11c).

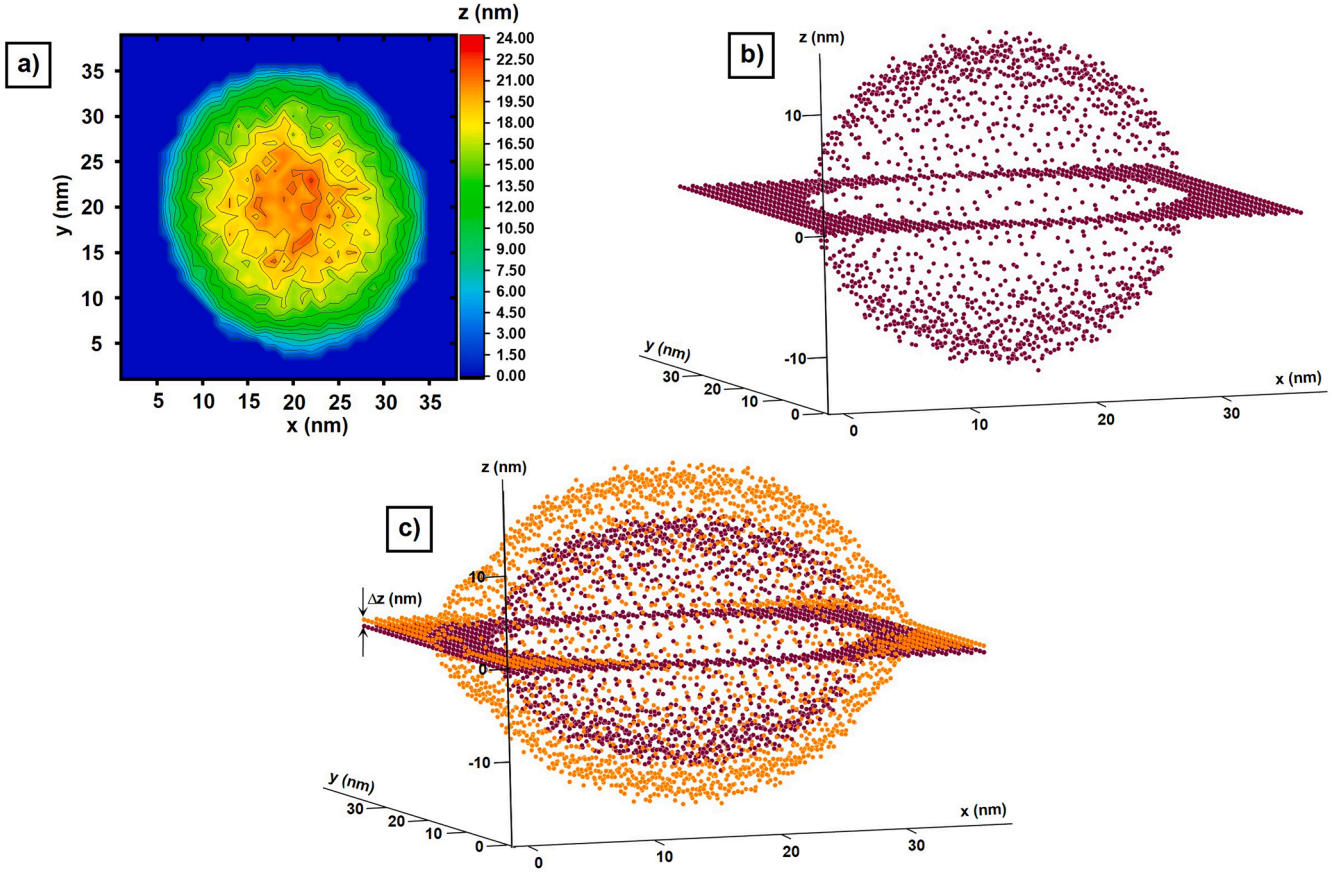


Fig. 11. $Au_{35}Co_{65}$ CS NP: a) thickness map of the nanoparticle Co core calculated using the $z^{Co-K-core}_{i,j}(nm)$ matrix; b) 3D shape reconstruction of the Co core performed with the $z^{Co-K-core}_{i,j}(nm)$ matrix and Eq. (61) (brown symbols); c) 3D shape reconstruction of the $Au_{56}Co_{44}$ alloyed shell determined by using $z^{Co-K-core}_{i,j}(nm)$, $z^t_{i,j}(nm)$ and Eq. (62); its outer surface is represented by the 3D shape of the entire particle (orange symbols), while its inner surface is defined by the 3D shape of the Co core (brown symbols) shifted down by $\Delta z = -0.7\ nm$ according to the tilt experiment. Points on the $z = 0$ and $z = -0.7\ nm$ planes are a drawing artifact that do not represent the 3D reconstructed shapes.

4. Conclusions

In this work, a thickness and 3D-shape reconstruction method for convex, z-symmetrical NPs with CS morphologies is proposed as an alternative to ET, which is based on the evaluation of a single 2D EDXS map without any tilt. The data analysis requires the quantitative evaluation of the measured characteristic X-ray intensities of chemical elements that are chosen for the reconstruction and their conversion into path-length matrices along the electron-beam direction based on calibration factors. The calibration factors depend not only on the chemical composition and the structure of the investigated material, but also on the TEM used to perform the experiment, i.e., the electron beam (electron energy, beam current, probe size) and the EDXS detector characteristics. This requires the measurement of at least one calibration factor for one chemical element for the used TEM/EDXS system. Based on that, theoretical calibration factors can be calculated for all other elements.

The 3D-shape reconstruction of NPs is symmetrically performed along the electron-beam direction z, which restricts the applicability of this method to convex, z-symmetrical NPs. NPs synthesized under equilibrium conditions are typically characterized by z-symmetrical, convex polyhedral/ellipsoidal shapes. Accordingly, the 3D reconstruction of the entire NP shape can be performed using a single EDXS map based on its 2D-projected shape on HAADF-STEM images. However, the 3D-shape reconstruction of non-equilibrium NPs and NP constituents (i.e. the core and the shell of CS NPs, even if the NPs are synthesized under equilibrium conditions) requires further investigation of the z-symmetry of NPs. This is possible by the acquisition of a single additional HAADF-STEM image of NPs at a given tilt angle to determine their z-symmetry and the shift of the NP core center relative to the entire NP.

The 3D-reconstruction method was applied to obtain the external shape and the shape of their morphologic constituents (i.e., the core and the shell) of a beam-sensitive CeO_2-CaF_2 CS NP with prismatic shape and an ellipsoidal $Au_{35}Co_{65}$ CS NP from their 2D EDXS maps. In the supporting information, further examples are presented, such as the thickness and the 3D-shape reconstruction of an amorphous SiO_2 NP and the thickness map of an alloyed $Pt_{61}Pd_{39}$ NP with irregular shape. In the ESI, equations are developed that allow the calculation of theoretical calibration factors for amorphous materials from those of the corresponding crystalline ones and to describe nanocrystalline/porose materials with different densities compared to those of their bulk (see ESI).

The proposed 3D-shape reconstruction method offers a viable and convenient addition to classical ET/MMT methods, when a tomography sample holder and/or the corresponding software are not available. It is especially useful to describe: 1) the 3D shape of NPs within agglomerates, which are located very close, but not overlapped with other NPs with the same chemical composition; 2) as an alternative to the classical ET to obtain the 3D shape of NPs located on substrates that contaminate and 3) to describe the 3D shape of morphologic constituents of a NP (core and shell), when these are composed of chemical elements with close atomic numbers, yielding about the same contrast on the HAADF-STEM images of an ET tilt series.

Funding sources

R.P. and Y.M.E. acknowledge financial support from the Deutsche Forschungsgemeinschaft (DFG, German Research Foundation) through the Collaborative Research center *"4f for Future"* (CRC 1573, project number 471424360), project A4.

CRediT authorship contribution statement

Radian Popescu: Writing – original draft, Visualization, Validation, Software, Project administration, Methodology, Investigation, Formal analysis, Conceptualization. **Dagmar Gerthsen:** Writing – review & editing, Validation, Supervision. **Simon Hettler:** Writing – review & editing, Validation, Resources, Investigation. **Martin Peterlechner:** Writing – review & editing, Validation. **Erich Müller:** Writing – review & editing, Validation. **Damien Hudry:** Writing – review & editing, Resources. **Yolita Maria Eggeler:** Writing – review & editing, Supervision, Project administration.

Declaration of competing interest

The authors declare that they have no known competing financial interests or personal relationships that could have appeared to influence the work reported in this paper.

Supplementary materials

Supplementary material associated with this article can be found, in the online version, at doi:10.1016/j.ultramic.2026.114466.

Data availability

Data will be made available on request.

References

[1] Y. Hao, S. Chen, X. Zhang, T. Chen, L-asparagine assisted synthesis of Pt/CeO_2 nanospheres for toluene combustion, Catalysts 12 (8) (2022) 887.
[2] C. Gao, F. Lyu, Y. Yin, Encapsulated metal nanoparticles for catalysis, Chem. Rev. 121 (2) (2021) 834–881.
[3] S.K. Murthy, Nanoparticles in modern medicine: state of the art and future challenges, Int. J. Nanomed. 2 (2) (2007) 129–141.
[4] V. Mazumder, Y. Lee, S. Sun, Recent development of active nanoparticle catalysts for fuel cell reactions, Adv. Funct. Mater. 20 (2010) 1224–1231.
[5] J.N. Freitas, A.S. Gonçalves, A.F. Nogueira, A comprehensive review of the application of chalcogenide nanoparticles in polymer solar cells, Nanoscale 6 (2014) 6371–6397.
[6] M. Gu, Q. Zhang, S. Lamon, Nanomaterials for optical data storage, Nat. Rev. Mater. 1 (2016) 16070.
[7] F. Zhu, J. Kim, K.-C. Tsao, J. Zhang, H. Yang, Recent development in the preparation of nanoparticles as fuel cell catalysts, Curr. Opin. Chem. Eng. 8 (2015) 89–97.
[8] J. Reguera, D.J. de Aberasturi, N. Winckelmans, J. Langer, S. Bals, L.M. Liz-Marzan, Synthesis of Janus plasmonic–magnetic, star–sphere nanoparticles, and their application in SERS detection, Faraday Discuss. 191 (2016) 47–59.
[9] P. Midgley, M. Weyland, 3D electron microscopy in the physical sciences: the development of Z-contrast and EFTEM tomography, Ultramicroscopy 96 (3–4) (2003) 413–431.
[10] P. Midgley, R. Dunin-Borkowski, Electron tomography and holography in materials science, Nat. Mater. 8 (4) (2009) 271–280.
[11] K. Jenkinson, L.M. Liz-Marzán, S. Bals, Multimode electron tomography sheds light on synthesis, structure and properties of complex metal-based nanoparticles, Adv. Mater. 34 (2022) 2110394.
[12] M. Radermacher, Electron Tomography (Ed: J. Frank), Springer US, Boston, MA, USA 1992, pp. 91–115.
[13] P. Gilbert, Iterative methods for the three-dimensional reconstruction of an object from projections, J. Theor. Biol. 36 (1972) 105–117.
[14] T.K. Moon, The expectation-maximization algorithm, IEEe Signal. Process. Mag. 13 (6) (1996) 47–60.
[15] B. Goris, W. Van den Broek, K.J. Batenburg, H.H. Mezerji, S. Bals, Electron tomography based on a total variation minimization reconstruction technique, Ultramicroscopy. 113 (2012) 120–130.
[16] K.J. Batenburg, S. Bals, J. Sijbers, C. Kübel, P.A. Midgley, J.C. Hernandez, U. Kaiser, E.R. Encina, E.A. Coronado, G. Van Tendeloo, 3D imaging of nanomaterials by discrete tomography, Ultramicroscopy 109 (2009) 730–740.
[17] P. Burdet, Z. Saghi, A.N. Filippin, A. Borrás, P.A. Midgley, A novel 3D absorption correction method for quantitative EDX-STEM tomography, Ultramicroscopy 160 (2016) 118–129.
[18] https://www.pubcompare.ai/product/1iPhCZIBPBHhf-iFtF7M/(Accessed on July 22, 2025); https://www.thermofisher.com/de/de/home/electron-microscopy/products/transmission-electron-microscopes/spectra-ultra-tem.html (Accessed on January 14, 2026).
[19] X. Duan, Y. Han, B. Zhu, Y. Gao, Modelling of metal nanoparticles' structures and dynamics under reaction conditions, Mater. Today Catal. 3 (2023) 100032.
[20] I. Lisiecki, Size, shape, and structural control of metallic nanocrystals, J. Phys. Chem. B 109 (2005) 12231–12244.
[21] A. Filankembo, S. Giorgio, I. Lisiecki, M.P. Pileni, Is the anion the major parameter in the shape control of nanocrystals? J. Phys. Chem. B 107 (2003) 7492–7500.
[22] C. Liu, Z. Ou, F. Guo, B. Luo, W. Chen, L. Qi, Q. Chen, Colloid−atom duality" in the assembly dynamics of Concave gold nanoarrows, J. Am. Chem. Soc. 142 (2020) 11669–11673.
[23] M. Li, T. Wu, H. Wang, H. Wan, X. Chen, H. Wang, Y. Wang, Atomic insights into dynamic integration of morphology and surface chemistry on the growth

mechanism of ternary Pt-based nanocatalysts, Cell Reports Phys. Sci. 6 (2025) 102396, 1-9.
[24] G. Cliff, G.W. Lorimer, The quantitative analysis of thin specimens, J. Microsc. 103 (2) (1975) 203–207.
[25] Standard library of the ESPRIT 2.3 software containing Cliff-lorimer factors for the Osiris microscope operated at 200 keV electron energy and equipped with a Super-X EDXS system experimentally used: the 200keV_Osiris(mod.Esl file). 2018.
[26] Z. Chen, M. Weyland, X. Sang, W. Xu, J.H. Dycus, J.M. LeBeau, A.J. D'Alfonso, L. J. Allen, S.D. Findlay, Quantitative atomic resolution elemental mapping via absolute-scale energy dispersive X-ray spectroscopy, Ultramicroscopy 168 (2016) 7–16.
[27] D.M. Longo, J.M. Howe, W.C. Johnson, Experimental method for determining Cliff-Lorimer factors in transmission electron microscopy (TEM) utilizing stepped wedge-shaped specimens prepared by focused ion beam (FIB) thinning, Ultramicroscopy 80 (1999) 85–97.
[28] R. Conconi, G. Ventruti, F. Nieto, G. Capitani, TEM-EDS microanalysis: comparison among the standardless, Cliff & Lorimer and absorption correction quantification methods, Ultramicroscopy 254 (2023) 113845.
[29] M. Watanabe, D. Williams, The quantitative analysis of thin specimens: a review of progress from the Cliff-Lorimer to the new ζ-factor methods, J. Microsc. 221 (2) (2006) 89–109.
[30] D. Meng, R. Popescu, C.M. Andrei, J. Himbert, E. Madirov, J.A. Branson, E. M. Reynolds, T. Prüßmann, J. Göttlicher, T. Vitova, N. Hildebrandt, Y.M. Eggeler, B.S. Richards, O. Walter, D. Hudry, Controlled synthesis of a new class of heterostructured metal oxides (Cerium, Thorium, Uranium)/calcium fluoride core-shell nanocrystals with atomically coherent interfaces, Angew. Chem., Int. Ed. 65 (2026) e24282, 1-7.
[31] F.A. Cardona, N. Jain, R. Popescu, D. Busko, E. Madirov, B.A. Arús, D. Gerthsen, A. De Backer, S. Bals, O.T. Bruns, A. Chmyrov, S. Van Aert, B.S. Richards, D. Hudry, Preventing cation intermixing enables 50% quantum yield in sub-15 nm short-wave infrared-emitting rare-earth based core-shell nanocrystals, Nat. Comm. 14 (2023) 4462–4476.
[32] D. Hudry, I.A. Howard, R. Popescu, D. Gerthsen, B.S. Richards, Structure–Property relationships in lanthanide-doped upconverting nanocrystals: recent advances in understanding core–Shell structures, Adv. Mater. 31 (2019) 1900623, 1-25.